J. Fluid Mech. (2024), *vol*. 987, A12, doi:10.1017/jfm.2024.398

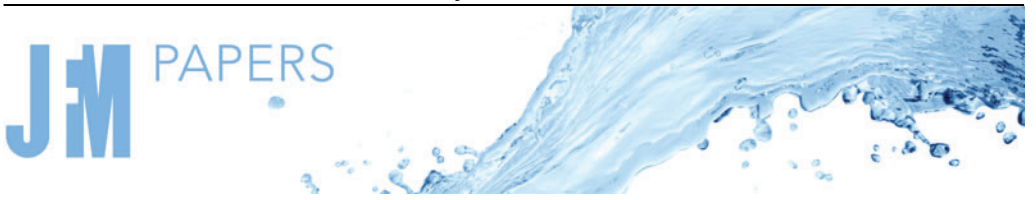

Stability of Stuart vortices in rotating stratified fluids

Yuji Hattori[1],† **and Makoto Hirota**[1]

[1]Institute of Fluid Science, Tohoku University, Sendai 980–8577, Japan

(Received 15 November 2023; revised 11 March 2024; accepted 11 April 2024)

The linear stability of the Stuart vortices, which is a model of arrays of vortices often observed in the atmosphere and the oceans, in rotating stratified fluids is investigated by local and modal stability analysis. As in the case of the two-dimensional (2-D) Taylor–Green vortices, five types of instability appear in general: the pure-hyperbolic instability, the strato-hyperbolic instability, the rotational-hyperbolic instability, the centrifugal instability and the elliptic instability. The condition for each instability and the estimate of the growth rate derived by Hattori & Hirota (*J. Fluid Mech.*, vol. 967, 2023, A32) are shown to also be useful for the Stuart vortices, which supports their applicability to general flows. The properties of each instability depend on stratification and rotation in a way similar to the case of the 2-D Taylor–Green vortices. For the Stuart vortices, however, the centrifugal instability and the elliptic instability become more dominant than the three hyperbolic instabilities in comparison to the 2-D Taylor–Green vortices; this is explained by the larger ratios of the maximum vorticity and the strain rate at the elliptic stagnation points to the strain rate at the hyperbolic stagnation points. Direct correspondence between the modal and local stability results is further established by comparing unstable modes to solutions to the local stability equations; this is useful for identifying the types of modes since the mechanism of instability is readily known in the local stability analysis. This helps us to discover the modes of the ring-type elliptic instability, which have been predicted only theoretically.

Key words: vortex instability, rotating flows, stratified flows

1. Introduction

Systems of large-scale vortices such as a vortex pair and an array of vortices are often observed in the atmosphere of the Earth and other planets, such as Jupiter and Saturn, and in the oceans (Thorpe 2005). For example, an array of counter-rotating vortices resembling a von Kármán vortex street is often observed in the wake of an isolated island (Etling 1989;

† Email address for correspondence: hattori@ifs.tohoku.ac.jp

Potylitsin & Peltier 1998). On Jupiter, anticyclones and cyclones formed a von Kármán vortex street for about 50 years (Youssef & Marcus 2003). These arrays of vortices can be generated by instabilities of a jet flow and a shear flow (the Kelvin–Helmholtz instability), the baroclinic instability and other mechanisms. The instability of an array of vortices, which is sometimes regarded as a secondary instability, is one of the most fundamental properties that are indispensable for understanding its dynamics and fate. The effect of rotation and stratification on the instability is of great interest because, for example, it can lead to preference in the sense of rotation of the vortices; in fact, the von Kármán vortex street in the wake of an isolated island sometimes becomes asymmetric, with anticyclonic vortices being nearly destroyed (Potylitsin & Peltier 1998; Stegner, Pichon & Beunier 2005).

There exist several types of instability in the vortices in rotating stratified fluids: the elliptic instability (Miyazaki & Fukumoto 1992; Miyazaki 1993; Leblanc & Cambon 1998; Leweke & Williamson 1998; Miyazaki & Adachi 1998; Leblanc 2000; Otheguy, Billant & Chomaz 2006*a*; Le Dizès 2008; Aspden & Vanneste 2009; Guimbard *et al.* 2010), the centrifugal instability (Rayleigh 1917; Kloosterziel & van Heijst 1991; Leblanc & Cambon 1998; Potylitsin & Peltier 1998, 1999), the zigzag instability (Billant 2000; Billant & Chomaz 2000*a*,*b*,*c*; Otheguy, Billant & Chomaz 2006*b*; Deloncle, Billant & Chomaz 2008; Waite & Smolarkiewicz 2008; Billant *et al.* 2010) and the radiative instability (Le Dizès & Billant 2009), while the transient growth (Arratia, Caulfield & Chomaz 2013; Gau & Hattori 2014) is also sometimes important. One of the important characteristics of the arrays of vortices is that there exist hyperbolic points, which add the hyperbolic instability to the above list of instabilities. The hyperbolic instability can be further classified into the pure-hyperbolic instability (Friedlander & Vishik 1991; Lifschitz & Hameiri 1991; Sipp & Jacquin 1998; Pralits, Giannetti & Brandt 2013), the strato-hyperbolic instability (Suzuki, Hirota & Hattori 2018; Hattori *et al.* 2021) and the rotational-hyperbolic instability (Sipp, Lauga & Jacquin 1999; Godeferd, Cambon & Leblanc 2001; Hattori & Hirota 2023).

The stability of arrays of vortices has been investigated by several authors. Leblanc & Cambon (1998) investigated the linear stability of the Stuart vortices in rotating non-stratified fluids by numerical analysis; the centrifugal, elliptic and pure-hyperbolic instabilities were found. Leblanc & Godeferd (1999) showed the structures of a mode of the pure-hyperbolic instability in the two-dimensional (2-D) Taylor–Green vortices by direct numerical simulation. Potylitsin & Peltier (1998) investigated the stability of periodic vortices in rotating stratified fluids by numerical analysis; the base flow is a quasi-steady state obtained by relaxation at low Reynolds numbers. According to them, anticyclonic vortices are strongly destabilized by weak rotation, but stabilized by strong rotation; they also claimed that strong stratification stabilizes the vortices. These results were obtained from numerical simulations with limited resolution at low Reynolds numbers. Potylitsin & Peltier (1999) investigated the stability of the Stuart vortices in rotating non-stratified fluids by numerical analysis. Three types of instability were found: the elliptic, the centrifugal and the (pure) hyperbolic instabilities.

In our previous work (Hattori *et al.* 2021), the linear stability of a periodic array of vortices in non-rotating stratified fluids has been investigated in detail; the effects of rotation were studied in Hattori & Hirota (2023), while the base flow was fixed to the 2-D Taylor–Green vortices. The latter work revealed several important aspects of the stability of a periodic array of vortices in rotating stratified fluids. Five types of instability have been shown to appear in general: the pure-hyperbolic instability, the strato-hyperbolic instability, the rotational-hyperbolic instability, the centrifugal instability and the elliptic instability. The condition for each instability and the estimate of the growth rate were

obtained in the framework of local stability analysis and proved useful in predicting which instability is dominant for a given set of parameters. However, our understanding is still incomplete because the above results were limited to a particular base flow. Further studies are needed to explore how the stability properties depend on multiple key parameters: the rotation rate of the system, the strength of stratification and the vorticity distribution, which is partially characterized by the strain rates at the stagnation points and the maximum vorticity.

In this paper, we study the linear stability of the Stuart vortices in rotating stratified fluids. We clarify how the growth rate and other characteristics of the instability depend on rotation, stratification and vorticity distribution. There are important reasons for studying the stability of the Stuart vortices after our detailed stability analysis of the 2-D Taylor–Green vortices (Hattori & Hirota 2023). First, the Stuart vortices are often regarded as a model of vortices that develop in a mixing layer as a result of the Kelvin–Helmholtz instability; understanding the stability of the Stuart vortices should be important because mixing layers are observed frequently in the atmosphere and the oceans. Next, it is important to investigate how the opposite-signed vortices, which exist in the 2-D Taylor–Green vortices but do not in the Stuart vortices, affect the stability properties. Finally, the instability condition and the estimate of the growth rate derived for each instability in Hattori & Hirota (2023) has been shown to be effective only for the 2-D Taylor–Green vortices; they should be tested for a different base flow that has different magnitudes of strain rates and vorticity, to show their applicability to general base flows. Although there are several works on the stability of the Stuart vortices with or without rotation (Pierrehumbert & Widnall 1982; Leblanc & Cambon 1998; Potylitsin & Peltier 1999; Godeferd *et al.* 2001), there is no work on the effects of stratification on the stability of the Stuart vortices. The stability of Kelvin–Helmholtz billows in stratified fluids was studied by Aravind, Dubos & Mathur (2022); in their work, however, the vorticity of the base flow and the gravity force are orthogonal, while they are parallel in the present work. We also show the existence of an unstable mode predicted only by theory (the 'ring mode' of the elliptic instability; Le Dizès 2008).

This paper is organized as follows. In § 2 the problem is formulated; concise expressions for the instability conditions and the estimates of the growth rates, which have been introduced in Hattori & Hirota (2023) in the framework of local stability analysis, are also summarized briefly. The methods of the numerical stability analysis are explained in § 3. The results of local and modal stability analysis are presented together with their comparison in § 4. We conclude in § 5.

2. Problem formulation

2.1. *Governing equations*

We consider the linear stability of the Stuart vortices in stably stratified and rotating fluids. The Stuart vortices are a one-dimensional array of periodic vortices with vorticity of the same sign (figure 1). The streamfunction and the vorticity are

$$\psi = \log\left(C\cosh y + \sqrt{C^2-1}\cos x\right), \tag{2.1}$$

$$\boldsymbol{\omega}_b = \omega_b(x,y)\,\boldsymbol{e}_z, \quad \omega_b(x,y) = -\frac{1}{\left(C\cosh y + \sqrt{C^2-1}\cos x\right)^2}, \tag{2.2a,b}$$

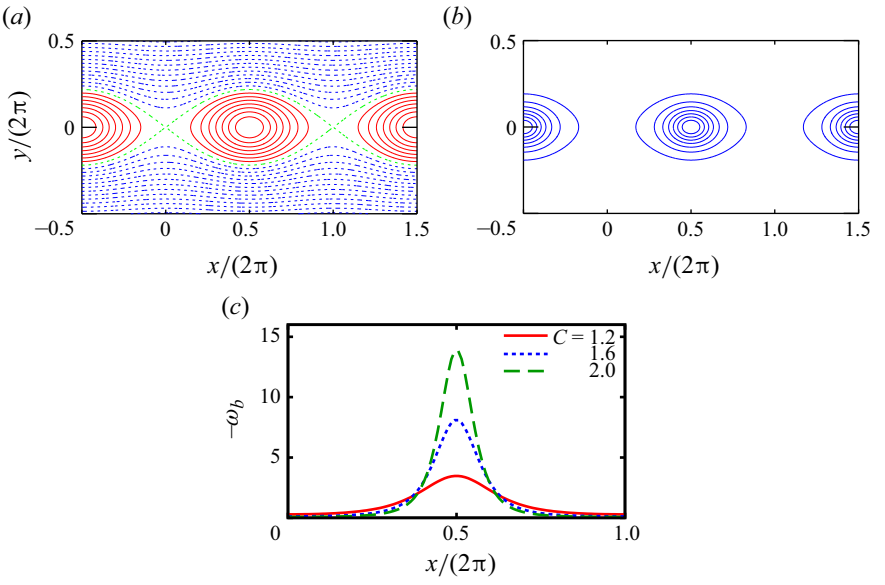

Figure 1. Stuart vortices: (*a*) streamlines and (*b*) contours of vorticity distribution for $C = 1.2$; (*c*) comparison of vorticity distribution on $y = 0$ between $C = 1.2$ (solid line), 1.6 (dotted line) and 2 (dashed line). In (*a*), the red, green and blue lines show the closed streamlines, the separatrix and the open streamlines, respectively.

where $C \geqslant 1$ is a constant. In the previous works (Leblanc & Cambon 1998; Godeferd *et al.* 2001), a different expression, $\psi = \log(\cosh y + \rho_s \cos x)$, is used instead of the above streamfunction; the two are related by $\rho_s = \sqrt{1 - C^{-2}}$, with a constant that does not affect the flow field. Two adjacent vortices are connected by a hyperbolic point. The vorticity is parallel to the vertical direction, which coincides with the direction of gravity force. The effects of density stratification are taken into account by the Boussinesq approximation. Then the Stuart vortices are steady in the absence of diffusion (Hattori & Hirota 2023).

Viscosity is taken into account in general, while diffusion of density is neglected since its effects are negligible (Hattori *et al.* 2021). The base flow is assumed steady because the growth of instabilities is much faster than the time evolution of the base flow due to viscous diffusion in the high-Reynolds-number flows considered in this paper. The velocity, pressure and density fields are decomposed as

$$\boldsymbol{u} = \boldsymbol{u}_b + \boldsymbol{u}', \tag{2.3}$$

$$p = p_b + p', \tag{2.4}$$

$$\rho = \rho_0 + \alpha z + \rho', \tag{2.5}$$

where $(\boldsymbol{u}_b, p_b, \rho_b = \rho_0 + \alpha z)$ and $(\boldsymbol{u}', p', \rho') = (u_x', u_y', u_z', p', \rho')$ are the base flow and the disturbance, the direction of the gravity force is taken as $-\boldsymbol{e}_z$, and the base density is assumed to be $\rho_b = \rho_0 + \alpha z$, with $\alpha = \partial\rho_b/\partial z < 0$ being a constant. The magnitude of the disturbance is infinitesimally small. Then the governing equations in non-dimensionalized

form are

$$\boldsymbol{\nabla}\cdot\boldsymbol{u}'=0, \tag{2.6}$$

$$\frac{\partial \boldsymbol{u}'}{\partial t}+(\boldsymbol{u}'\cdot\boldsymbol{\nabla})\boldsymbol{u}_b+(\boldsymbol{u}_b\cdot\boldsymbol{\nabla})\boldsymbol{u}'-\frac{1}{Ro}\,\boldsymbol{e}_z\times\boldsymbol{u}'=-\boldsymbol{\nabla}p'-\rho'\boldsymbol{e}_z+\frac{1}{Re}\,\nabla^2\boldsymbol{u}', \tag{2.7}$$

$$\frac{\partial \rho'}{\partial t}+(\boldsymbol{u}_b\cdot\boldsymbol{\nabla})\rho'-\frac{1}{F_h^2}\,u_z'=0, \tag{2.8}$$

where $Ro=U_0/(2\Omega_0 L_0)$ is the Rossby number, $Re=U_0L_0/\nu$ is the Reynolds number, $F_h=U_0/(L_0N)$ is the Froude number based on the horizontal scale, $N=\sqrt{-\alpha g/\rho_0}$ is the Brunt–Väisälä frequency, g is the acceleration of gravity, ν is the kinematic viscosity, Ω_0 is the angular velocity, and U_0 and L_0 are a characteristic velocity and a length scale, respectively. As in our previous works (Suzuki *et al.* 2018; Hattori *et al.* 2021), we set $L_0=2\pi$, which is the spatial period in the x direction, while U_0 is set to the maximum velocity 1. In the following, the values are scaled by U_0 and L_0 unless stated explicitly. It is pointed out that the minus sign of the Coriolis force in (2.7) is introduced because the vorticity distribution of the Stuart vortices in (2.2*a*,*b*) is negative; $Ro>0$ and $Ro<0$ correspond to the cyclonic and anticyclonic cases, respectively.

In the local stability analysis, the disturbance is assumed to be in the form of a wave packet:

$$\boldsymbol{u}'=\left(\hat{\boldsymbol{u}}_0+\delta\hat{\boldsymbol{u}}_1+\cdots\right)\exp\left(\frac{\mathrm{i}}{\delta}\,\Phi\right), \tag{2.9}$$

$$p'=\left(\hat{p}_0+\delta\hat{p}_1+\cdots\right)\exp\left(\frac{\mathrm{i}}{\delta}\,\Phi\right), \tag{2.10}$$

$$\rho'=\left(\hat{\rho}_0+\delta\hat{\rho}_1+\cdots\right)\exp\left(\frac{\mathrm{i}}{\delta}\,\Phi\right), \tag{2.11}$$

where δ is a small parameter, and Φ is eikonal, satisfying $\mathrm{D}\Phi/\mathrm{D}t=0$ (where $\mathrm{D}/\mathrm{D}t=\partial/\partial t+\boldsymbol{u}_b\cdot\boldsymbol{\nabla}$). Viscosity is neglected in the local stability analysis. Substituting the above expressions into (2.6)–(2.8) yields a set of ordinary differential equations at the leading order:

$$\frac{\mathrm{d}\boldsymbol{X}}{\mathrm{d}t}=\boldsymbol{U}(\boldsymbol{X}), \tag{2.12}$$

$$\frac{\mathrm{d}\boldsymbol{k}}{\mathrm{d}t}=-\boldsymbol{L}^{\mathrm{T}}\boldsymbol{k}, \tag{2.13}$$

$$\frac{\mathrm{d}\boldsymbol{a}}{\mathrm{d}t}=\left(2\hat{\boldsymbol{k}}\hat{\boldsymbol{k}}^{\mathrm{T}}-\boldsymbol{I}\right)\boldsymbol{L}\boldsymbol{a}+\left(\hat{\boldsymbol{k}}\hat{\boldsymbol{k}}^{\mathrm{T}}-\boldsymbol{I}\right)r\boldsymbol{e}_z-\frac{1}{Ro}\left(\hat{\boldsymbol{k}}\hat{\boldsymbol{k}}^{\mathrm{T}}-\boldsymbol{I}\right)\boldsymbol{e}_z\times\boldsymbol{a}, \tag{2.14}$$

$$\frac{\mathrm{d}r}{\mathrm{d}t}=\frac{1}{F_h^2}\,a_z, \tag{2.15}$$

where $\boldsymbol{L}_{ij}=\partial U_i/\partial x_j$ and $\hat{\boldsymbol{k}}=\boldsymbol{k}/|\boldsymbol{k}|$ (Friedlander & Vishik 1991; Lifschitz & Hameiri 1991; Leblanc 1997). Here, $\boldsymbol{X}$ is the position of the fluid particle, and $\boldsymbol{k}=\boldsymbol{\nabla}\Phi$ is the local wavevector, while $\boldsymbol{a}=\hat{\boldsymbol{u}}_0$ and $r=\hat{\rho}_0$ are the amplitudes of the disturbance corresponding to velocity and density, respectively. The incompressibility condition (2.6) leads to $\boldsymbol{a}\cdot\boldsymbol{k}=0$, which is satisfied for $t>0$ if it holds at $t=0$. The base flow is unstable if the amplitude $\{\boldsymbol{a},r\}$ grows without bound.

The number of variables in (2.14) and (2.15) can be reduced from four to three by introducing

$$p = \frac{k}{k_\perp}\boldsymbol{k}_\perp \cdot \boldsymbol{a}_\perp = -\frac{kk_z}{k_\perp}a_z, \quad q = \left(\frac{k}{k_\perp}\boldsymbol{k}_\perp \times \boldsymbol{a}_\perp\right)\cdot \boldsymbol{e}_z, \quad s = \frac{k}{k_\perp}r \tag{2.16a–c}$$

as in Bayly, Holm & Lifschitz (1996), where $\boldsymbol{k}_\perp = (k_x, k_y)^{\mathrm{T}}$, $\boldsymbol{a}_\perp = (a_x, a_y)^{\mathrm{T}}$ and

$$\boldsymbol{L} = \begin{pmatrix} \boldsymbol{L}_\perp & 0 \\ 0 & 0 \end{pmatrix}, \quad \boldsymbol{H} = \boldsymbol{L}_\perp \begin{pmatrix} 0 & 1 \\ -1 & 0 \end{pmatrix}. \tag{2.17a,b}$$

Then the equations (2.14) and (2.15) reduce to

$$\frac{\mathrm{d}}{\mathrm{d}t}\begin{pmatrix} p \\ q \\ s \end{pmatrix} = \begin{pmatrix} \dfrac{\mathrm{d}}{\mathrm{d}t}\log\dfrac{|\boldsymbol{k}_\perp|}{|\boldsymbol{k}|} & \dfrac{2k_z^2\boldsymbol{H}\boldsymbol{k}_\perp\cdot\boldsymbol{k}_\perp}{|\boldsymbol{k}|^2\,|\boldsymbol{k}_\perp|^2} + \dfrac{k_z^2}{Ro\,k^2} & \dfrac{|\boldsymbol{k}_\perp|^2}{|\boldsymbol{k}|^2}k_z \\ -\omega_z - Ro^{-1} & -\dfrac{\mathrm{d}}{\mathrm{d}t}\log\dfrac{|\boldsymbol{k}_\perp|}{|\boldsymbol{k}|} & 0 \\ -\dfrac{1}{F_h^2 k_z} & 0 & -\dfrac{\mathrm{d}}{\mathrm{d}t}\log\dfrac{|\boldsymbol{k}_\perp|}{|\boldsymbol{k}|} \end{pmatrix}\begin{pmatrix} p \\ q \\ s \end{pmatrix}. \tag{2.18}$$

2.2. *Instability condition and estimate of growth rates*

Here, we summarize the condition and the estimate of the growth rate for each instability obtained in the framework of local stability analysis; see Hattori & Hirota (2023) for the details. It is pointed out that our aim here is to give compact and useful expressions for the instability condition and the growth rate for each instability, which are not always rigorous but allow us to interpret the results in § 4 without difficulties. In the following, C_{PH}, C_{SH}, C_{RH}, C_C and C_E are $O(1)$ coefficients that depend on the parameters in general; the actual dependence will be checked numerically in § 4.1 (figure 8).

(i) Pure-hyperbolic instability. The pure-hyperbolic (PH) instability is due to stretching near the hyperbolic stagnation points. It occurs when

$$|Ro^{-1}| < \varepsilon_h. \tag{2.19}$$

The growth rate is estimated as

$$\sigma = C_{PH}\left(\varepsilon_h^2 - Ro^{-2}\right)^{1/2}. \tag{2.20}$$

(ii) Strato-hyperbolic instability. The strato-hyperbolic (SH) instability is a variant of the pure-hyperbolic instability under stratification effects. It occurs when the exponential growth near the hyperbolic stagnation points is connected with phase shift due to the inertia-gravity waves in favour of exponential growth. It occurs when

$$|Ro^{-1}| < \varepsilon_h \quad \text{and} \quad F_h^{-1} \gtrsim \omega_{max}/2. \tag{2.21a,b}$$

The growth rate is estimated as

$$\sigma = C_{SH}\left(\varepsilon_h^2 - Ro^{-2}\right)^{1/2}. \tag{2.22}$$

Base flow	ε_h	ε_e	ω_{max}
Stuart, $C = 1.2$	3.14	3.14	21.8
Stuart, $C = 1.6$	3.14	3.14	51.0
Stuart, $C = 2$	3.14	3.14	87.5
2-D Taylor–Green, $\varepsilon_e/\omega_{max} = 0$ (HH2023)	3.14	0	6.28
2-D Taylor–Green, $\varepsilon_e/\omega_{max} = 0.2$ (HH2023)	2.88	1.26	6.28

Table 1. Strain rates at hyperbolic and elliptic stagnation points, and maximum vorticity of the Stuart vortices considered in the present paper. The values for the 2-D Taylor–Green vortices studied in Hattori & Hirota (2023) (HH2023) are also included for comparison.

(iii) Rotational-hyperbolic instability. The rotational-hyperbolic (RH) instability is also a variant of the pure-hyperbolic instability. It occurs when

$$|Ro^{-1}| \gtrsim \varepsilon_h. \tag{2.23}$$

The growth rate is estimated as

$$\sigma = C_{RH}\varepsilon_h. \tag{2.24}$$

(iv) Centrifugal instability. The essential mechanism of the centrifugal (C) instability was given by Rayleigh (1917). It occurs when positive energy is released by interchanging fluid elements under conservation of angular momentum. Assuming a monotonically decreasing vorticity distribution, the instability condition turns out to be

$$-\omega_{max} < Ro^{-1} < 0. \tag{2.25}$$

The growth rate is estimated as

$$\sigma = C_C\omega_{max}. \tag{2.26}$$

(v) Elliptic instability. The elliptic (E) instability is caused by resonance due to strain at elliptic stagnation points. It occurs when

$$F_h^{-1} < \tfrac{1}{2}\omega_{max} \quad \text{and} \quad Ro^{-1} < -\tfrac{3}{2}\omega_{max} \text{or } Ro^{-1} > -\tfrac{1}{2}\omega_{max}, \tag{2.27a,b}$$

or

$$F_h^{-1} > \tfrac{1}{2}\omega_{max} \quad \text{and} \quad -\tfrac{3}{2}\omega_{max} < Ro^{-1} \lesssim 0. \tag{2.28a,b}$$

The growth rate is estimated as

$$\sigma = C_E\varepsilon_e. \tag{2.29}$$

The coefficient C_E can be expressed as a function of F_h and Ro at the elliptic stagnation point (Leblanc 2000).

The values of the strain rates ε_h and ε_e at the hyperbolic and elliptic stagnation points, respectively, and the maximum magnitude of vorticity ω_{max}, which appear in the expressions above, are listed in table 1, which includes those for the 2-D Taylor–Green vortices considered in Hattori & Hirota (2023) for comparison purposes. It is pointed out that ω_{max} and ε_e of the Stuart vortices are larger than values for the 2-D Taylor–Green vortices, while ε_h is not much different between the two base flows.

3. Numerical procedure

3.1. *Local stability analysis*

The numerical method for local stability analysis is same as that in Hattori & Hirota (2023). Equations (2.12)–(2.15) were integrated by the fourth-order Runge–Kutta method. We consider periodic orbits of fluid particles throughout this paper. We also assume that the wavevector $\boldsymbol{k}$ is time-periodic, which is a necessary condition for exponential instability on the periodic orbits. It is known that $\boldsymbol{k}$ is time-periodic if it is perpendicular to the streamline initially (Lifschitz & Hameiri 1993; Hattori & Fukumoto 2003):

$$\boldsymbol{k}(0) \cdot \boldsymbol{u}_b(\boldsymbol{X}(0)) = 0. \tag{3.1}$$

Then the time evolution of amplitude is described by a Floquet matrix $\boldsymbol{F}$ since the matrices that appear in (2.14) are also time-periodic:

$$\{\boldsymbol{a}, r\}(t+T) = \boldsymbol{F}(T)\,\{\boldsymbol{a}, r\}(t), \tag{3.2}$$

where T is the period of $\boldsymbol{k}$ that coincides with that of the particle motion $\boldsymbol{X}$ (Lifschitz & Hameiri 1993; Hattori & Fukumoto 2003). Our task is to calculate the eigenvalues $\{\mu_i\}$ of $\boldsymbol{F}(T)$, which determines the growth rate as

$$\sigma_i = \frac{\log|\mu_i|}{T}. \tag{3.3}$$

The initial conditions should be specified to have particular solutions for a given set of the Rossby number Ro and the Froude number F_h. One parameter, which is denoted by β in the following subsections, is required for $\boldsymbol{X}(0)$ to identify a streamline in a 2-D flow. We set

$$\boldsymbol{X}(0) = (\pi, \beta y_c, 0)^{\mathrm{T}}, \tag{3.4}$$

where $y_c = \cosh^{-1}(1 + 2\sqrt{1 - C^{-2}})$ is the maximum of y on the separatrix. The elliptic stagnation point corresponds to $\beta = 0$, while $\beta = 1$ corresponds to the separatrix. The open streamlines corresponding to $\beta > 1$ are also considered.

Another parameter is required for $\boldsymbol{k}(0)$ to specify the direction of the wavevector that satisfies (3.1); we take the angle between $\boldsymbol{e}_z$ and $\boldsymbol{k}(0)$, which is denoted by θ_0. It should be pointed out that the magnitude of $\boldsymbol{k}(0)$ is arbitrary since the right-hand side of (2.14) depends only on the direction of $\boldsymbol{k}$ and is independent of the magnitude after taking the short-wave limit. For the amplitudes $\boldsymbol{a}(0)$ and $r(0)$, three independent initial conditions satisfying the incompressibility condition $\boldsymbol{a}(0) \cdot \boldsymbol{k}(0) = 0$ are considered; the results do not depend on the choice of the initial conditions since the space spanned by the three initial conditions is common. As a result, we obtain the largest growth rate σ as a function of β, θ_0, Ro and F_h, namely $\sigma = \sigma(\beta, \theta_0, Ro, F_h)$.

3.2. *Modal stability analysis*

In the modal stability analysis, (2.6)–(2.8) were solved numerically by the Fourier spectral method (Peyret 2010), assuming periodic boundary conditions in all three directions as in Hattori *et al.* (2021) and Hattori & Hirota (2023). Since the Stuart vortices are periodic in x but not in y, the vortices are placed at $y = nL_y$, and those with the opposite-signed vorticity are placed at $y = (n + 1/2)L_y$, for $n = 0, \pm1, \pm2, \ldots$, to make the base flow periodic in y. The spatial period L_y is fixed at $L_y = 4L_0 = 8\pi$, which is large enough to make the effects of the periodic boundary condition in the y direction negligible (Hattori *et al.* 2021). The time marching was performed by the fourth-order Runge–Kutta method.

Since the base flow is 2-D, the time evolution of disturbances is separable in the vertical direction. Thus we set

$$\boldsymbol{u}' = \exp(\mathrm{i}[\mu(x/L_x) + k_z z]) \sum_{k_x=-K_x}^{K_x} \sum_{k_y=-K_y}^{K_y} \tilde{\boldsymbol{u}}_{k_x,k_y} \exp(\mathrm{i}[k_x(x/L_x) + k_y(y/L_y)]), \tag{3.5}$$

with similar expressions for p' and ρ'. In the above equation, we have included the Floquet exponent $\mathrm{i}\mu$ to consider Floquet modes in general. The number of the Fourier modes is 1024×4096, as in Hattori *et al.* (2021).

The growth rate and frequency were obtained by the method of Krylov subspaces (Edwards *et al.* 1994; Julien, Ortiz & Chomaz 2004; Donnadieu *et al.* 2009; Hattori *et al.* 2021; Hattori & Hirota 2023). Starting from randomized initial conditions, (2.6)–(2.8) were integrated for a certain long time. Intermediate states $\{(\boldsymbol{u}'(T_0), \rho'(T_0)), (\boldsymbol{u}'(T_0 + \Delta T), \rho'(T_0 + \Delta T)), \ldots, (\boldsymbol{u}'(T_0 + (N_K - 1)\,\Delta T), \rho'(T_0 + (N_K - 1)\,\Delta T))\}$ were used as generators of the Krylov subspace. Then the eigenvalues and the eigenmodes were obtained in the N_K-dimensional Krylov subspace. In this method, the error of an eigenvalue λ of a linear operator $\boldsymbol{L}$ can be evaluated by

$$\epsilon = \frac{\|\boldsymbol{L}\boldsymbol{v} - \lambda \boldsymbol{v}\|}{\|\boldsymbol{v}\|}, \tag{3.6}$$

where $\boldsymbol{v}$ is the corresponding approximate eigenvector. The error ϵ depends on the initial time of the data T_0, the interval between the data ΔT, and the dimension of the Krylov subspace N_K. In order to obtain eigenvalues accurately, several Krylov subspaces were generated from different sets of parameters, and the eigenvalue with the smallest error for each eigenmode was chosen. The actual values of the parameters were chosen after trial and error; N_K was 5, 10 or 20, and $T_0 = 92, 112, \ldots, 192$, while ΔT was fixed at 2. Typically, the error of the eigenvalue is $\epsilon = O(10^{-10})$ for the largest eigenvalue for a fixed wavenumber k_z, while it increases for subdominant eigenmodes. In the following, we discarded the eigenmodes with $\epsilon \geqslant 10^{-3}$.

It turned out that the growth rates of the cyclonic case are sometimes difficult to obtain because they are smaller than those of the anticyclonic case. Therefore, we applied a filter that damps the anticyclonic modes and keeps the cyclonic modes unchanged, to obtain the growth rates of the cyclonic case.

3.3. *Realizability as a mode*

As we will see later, in § 4, the instabilities that are found by local stability analysis are not always found in modal stability analysis at finite Reynolds numbers since high-wavenumber modes are damped by viscous damping. In this case, the corresponding region of the instability in the (β, θ_0) plane is often thin so that it is difficult to construct an unstable mode. We use the realizability introduced in Hattori & Hirota (2023),

$$\mathcal{R} = \int_S \sigma \sin\theta_0 \,\mathrm{d}\beta \,\mathrm{d}\theta_0, \tag{3.7}$$

where S is the region of an instability in the (β, θ_0) plane, to quantify the realizability as a mode of each instability. The idea behind the above definition is that the eigenmode corresponding to a wider unstable region in the (β, θ_0) plane is less affected by viscous damping because the corresponding mode also has a large spatial width and thereby the radial wavenumber of the mode is small.

4. Results

In this section, we show the results of local and modal stability analysis of the Stuart vortices in rotating stratified fluids. For the parameter C, which controls the core size of the vortices, we show most of the results for $C = 1.2$ and 2 to elucidate the dependence on C or the ratio of the strain rates at the stagnation points to the maximum vorticity, and to compare them to the results of our previous works (Suzuki *et al.* 2018; Hattori *et al.* 2021), while the results for $C = 1.6$ are also used to complement the dependence on C. The ratio of the strain rate at the elliptic stagnation points to the maximum vorticity is $\varepsilon_e/\omega_{max} = 0.144$, 0.062 and 0.036 for $C = 1.2$, 1.6 and 2, respectively (table 1).

4.1. *Results of local stability analysis*

First, we show the growth rate $\sigma(\beta, \theta_0, Ro, F_h)$ obtained by local stability analysis as a function of β and θ_0 for given values of Ro and F_h. Figure 2 shows the growth rate for $C = 1.2$ in the absence of stratification ($F_h^{-1} = 0$). The Rossby number is set to $Ro^{-1} = 0, \pm 2, \pm 5, \pm 10, \pm 15$. The streamlines outside the separatrix, which can be regarded as periodic modulo 2π in the x direction, are also considered as in Suzuki *et al.* (2018); the separatrix, which connects the hyperbolic stagnation points, corresponds to $\beta = 1$, while the inner and outer streamlines correspond to $0 \leqslant \beta < 1$ and $\beta > 1$, respectively.

In contrast to the case of the 2-D Taylor–Green vortices (Hattori & Hirota 2023), the pure-hyperbolic instability occurs in the absence of rotation (figure 2*a*); the region of the pure-hyperbolic instability, which is centred at $\beta = 1$, merges with that of the elliptic instability emanating from $(\beta, \theta_0) \approx (0, 60^\circ)$ (Suzuki *et al.* 2018). It is stabilized by rotation as the growth rate near $\beta = 1$ is much smaller for $Ro^{-1} = \pm 2$ (figures 2*b*,*c*) than for $Ro^{-1} = 0$ (figure 2*a*). As the anticyclonic rotation becomes strong, the region of the elliptic instability splits from the pure-hyperbolic instability (figure 2*b*); it approaches the vortex core, while the maximum growth rate at $\theta_0 = 0^\circ$ increases for $Ro^{-1} = -5$ and -10 (figures 2*d*,*f*); it is stabilized for $Ro^{-1} = -15$ (figure 2*h*). For cyclonic rotation, the region of the elliptic instability shrinks but survives with increasing Ro^{-1}, while the maximum growth rate decreases gradually (figures 2*c*,*e*,*g*,*i*). The centrifugal instability occurs only for the anticyclonic rotation as in the case of the 2-D Taylor–Green vortices (Hattori & Hirota 2023). The unstable region of the centrifugal instability is observed in $0.8 \lesssim \beta \lesssim 1$ for $Ro^{-1} = -2$ (figure 2*b*); it approaches the vortex core with increasing $|Ro^{-1}|$ as predicted by local stability analysis (Hattori & Hirota 2023) (figures 2*b*,*d*,*f*,*h*). The unstable region becomes narrow at $\beta \approx 0.4$ for $Ro^{-1} = -15$ (figure 2*h*). For $Ro^{-1} = 5, \pm 10, \pm 15$, thin regions of weak instability emanating from $(\beta, \theta_0) = (1, 90^\circ)$ are observed (figures 2*c*,*f*,*g*,*h*,*i*); they are due to the rotational-hyperbolic instability. The unstable region of the elliptic instability merges with that of the rotational-hyperbolic instability for $Ro^{-1} > 0$. The occurrence and the growth rate of the instabilities are in good agreement with prediction in § 2.2.

Figure 3 shows the growth rate for the Stuart vortices with $C = 2$ in the absence of stratification ($F_h^{-1} = 0$). The results are similar to the case $C = 1.2$ (figure 2). However, a few remarkable differences are observed: the regions of the pure-hyperbolic instability and the elliptic instability are almost separated at $Ro^{-1} = 0$ (figure 2*a*); the elliptic instability is not completely stabilized at $Ro^{-1} = -15$. Most importantly, the growth rate of the centrifugal instability is much larger than that for $C = 1.2$. These differences are consistent with the prediction in § 2.2 as the value $\omega_{max} = 87.5$ for $C = 2$ is much larger than

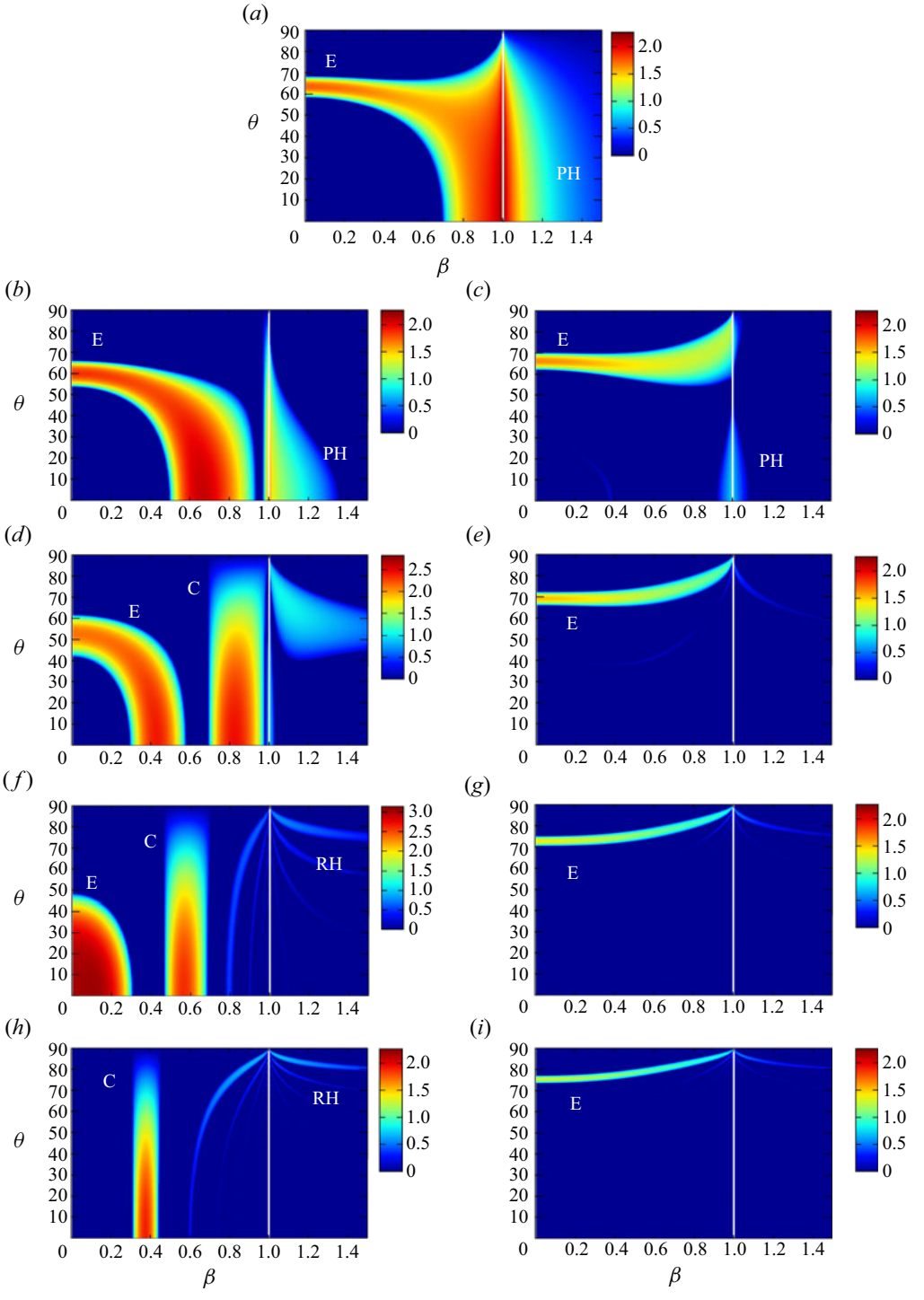

Figure 2. Growth rate $\sigma(\beta, \theta_0, Ro, F_h)$ as a function of β and θ_0 obtained by local stability analysis. Stuart vortices with $C = 1.2$ and $F_h^{-1} = 0$. The Ro^{-1} values are (*a*) 0, (*b*) −2, (*c*) 2, (*d*) −5, (*e*) 5, (*f*) −10, (*g*) 10, (*h*) −15, (*i*) 15.

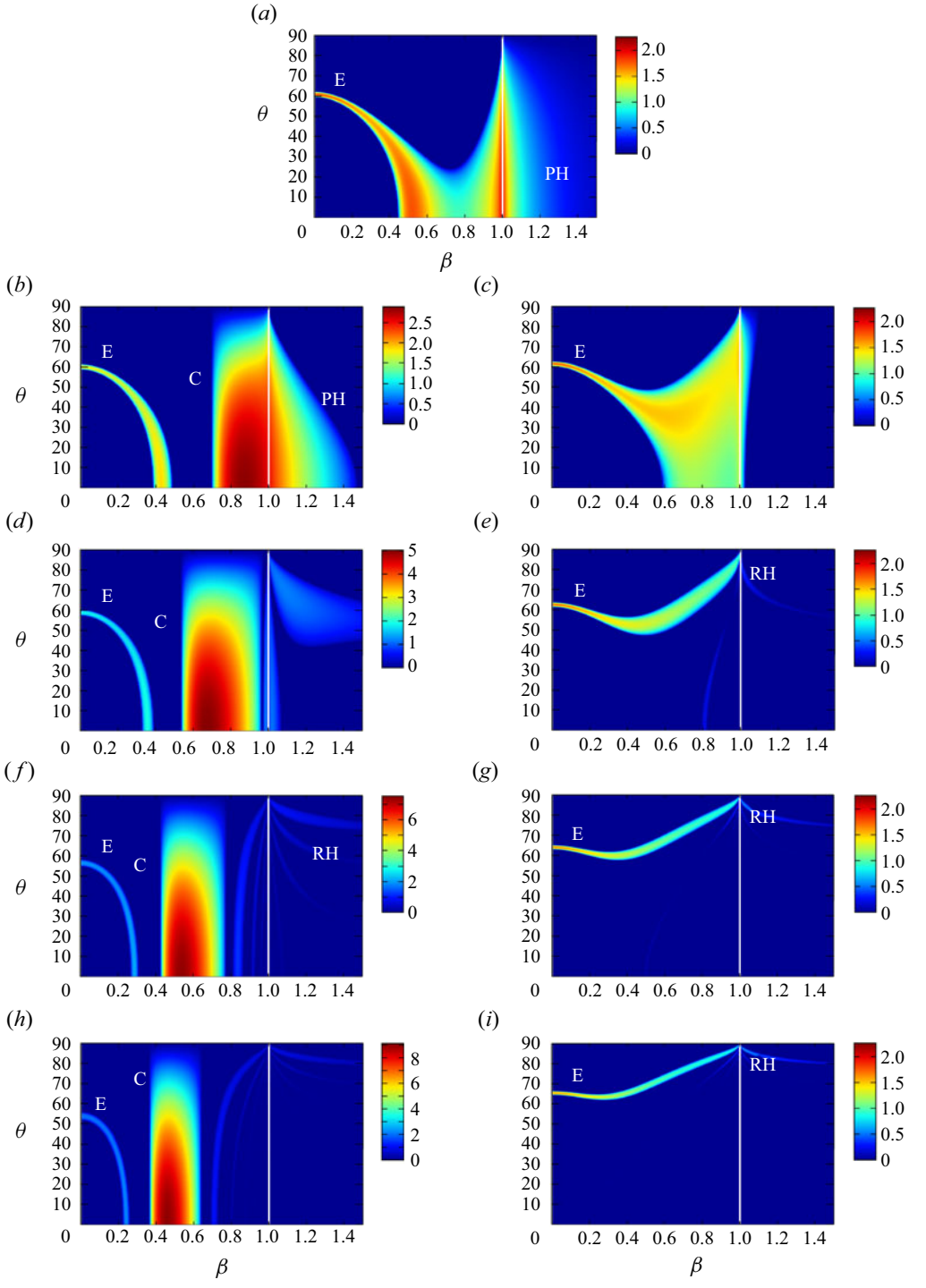

Figure 3. Growth rate $\sigma(\beta, \theta_0, Ro, F_h)$ as a function of β and θ_0 obtained by local stability analysis. Stuart vortices with $C = 2$ and $F_h^{-1} = 0$. The Ro^{-1} values are (*a*) 0, (*b*) −2, (*c*) 2, (*d*) −5, (*e*) 5, (*f*) −10, (*g*) 10, (*h*) −15, (*i*) 15.

$\omega_{max} = 21.8$ for $C = 1.2$; the elliptic instability occurs for $Ro^{-1} > -(1/2)\omega_{max} = -43.8$, while the growth rate of the centrifugal instability is $C_C\omega_{max}$, which is much larger than rates of other instabilities proportional to or smaller than ε_h or ε_e.

The results of stratified cases with $F_h^{-1} = 8$ are shown in figure 4 for $C = 1.2$, and figure 5 for $C = 2$, respectively. For $Ro^{-1} = 0$, the region of the pure-hyperbolic instability is restricted to $\theta_0 \lesssim 30^\circ$, while the regions of the strato-hyperbolic instability are observed near $\beta = 1$ at $\theta_0 \approx 40^\circ$ and 60° for $C = 1.2$ (figure 4*a*), and at $\theta_0 \approx 50^\circ$ for $C = 2$ (figure 5*a*). The pure-hyperbolic and strato-hyperbolic instabilities are also observed for $Ro^{-1} = \pm 2$ with reduced growth rate (figures 4*b*,*c* and 5*b*,*c*), but they are stabilized for $|Ro^{-1}| \geqslant 5$. For $C = 1.2$, the elliptic instability is not completely stabilized but weak at large θ_0 because $F_h^{-1} = 8$ is close to $(1/2)\omega_{max} = 10.9$, at which the condition for the elliptic instability changes; however, it survives near $\theta_0 = 0^\circ$, for which the effect of stratification is weak; it is observed in $0.5 \lesssim \beta \lesssim 0.9$, $0.3 \lesssim \beta \lesssim 0.6$ and $0 \lesssim \beta \lesssim 0.3$ for $Ro^{-1} = -2$, -5 and -10, respectively (figures 4*b*,*d*,*f*). For $C = 2$, the elliptic instability is not stabilized at large θ_0 since $F_h^{-1} = 8$ is much smaller than $(1/2)\omega_{max} = 43.8$, while the growth rate is reduced. The region of the centrifugal instability appears at the same position in β as for $F_h^{-1} = 0$, but shrinks to small θ_0 both for $C = 1.2$ and 2; however, the maximum growth rate is independent of stratification since it occurs at $\theta_0 = 0^\circ$. The rotational-hyperbolic instability is not observed since the growth rate is significantly reduced by stratification.

Next, we focus on the maximum growth rate for fixed magnitudes of rotation and stratification $\sigma_{max}(Ro, F_h) = \max_{\beta,\theta_0} \sigma(\beta, \theta_0, Ro, F_h)$ as in the case of the 2-D Taylor–Green vortices (Hattori & Hirota 2023). Figure 6 shows $\sigma_{max}(Ro, F_h)$ for $F_h^{-1} = 8$ as an example. It is pointed out that for $C = 1.2$, there are two lines of the elliptic instability for $-10.4 < Ro^{-1} < -1$ because there exist two extrema, one at $\beta = 0$ and the other at $\theta_0 = 0^\circ$, the latter being larger. For $C = 1.2$ (figure 6*a*), all instabilities except the rotational-hyperbolic instability appear as the most unstable instability in some intervals; the maximum growth rate for $F_h^{-1} = 8$ is due to the centrifugal instability in $Ro^{-1} < -13.2$ and $-6.8 < Ro^{-1} < -4.4$, the elliptic instability in $-13.2 < Ro^{-1} < -6.8$, $-4.4 < Ro^{-1} < -1.2$ and $1.4 < Ro^{-1}$, the pure-hyperbolic instability in $-1.2 < Ro^{-1} < 1.2$, and the strato-hyperbolic instability in $1.2 < Ro^{-1} < 1.4$. For $C = 2$ (figure 6*b*), the maximum growth rate is dominated by the centrifugal instability for $Ro^{-1} < 0$ as predicted in § 2.2, although a tiny region where the elliptic instability is maximum exists ($-0.6 < Ro^{-1} < -0.2$). For $Ro^{-1} > 0$, the pure-hyperbolic instability and the elliptic instability become maximum for $0 < Ro^{-1} < 1.8$ and $Ro^{-1} > 1.8$, respectively.

The effects of stratification on the maximum growth rate $\sigma_{max}(Ro, F_h)$ are shown in figure 7; the realizability $\mathcal{R}$ is also plotted against Ro^{-1}. The maximum growth rate is unaffected by stratification except that of the elliptic instability for $Ro^{-1} > 0$, which decreases with stratification. The realizability decreases with stratification for all instabilities, but for the elliptic instability for $-13.2 < Ro^{-1} < -6.8$, $\mathcal{R}$ becomes maximum at $F_h^{-1} = 10 \approx \omega_{max}/2$ as the unstable region expands to large θ_0. It is pointed out that although the growth rate of the centrifugal instability increases with the magnitude of rotation for $C = 2$, the realizability decreases with $|Ro^{-1}|$ for strong rotation; the maximum of the growth rate would be at $Ro^{-1} \approx -30$. The centrifugal instability is stabilized at $Ro^{-1} = \omega_{max} = -87.5$ according to (2.25).

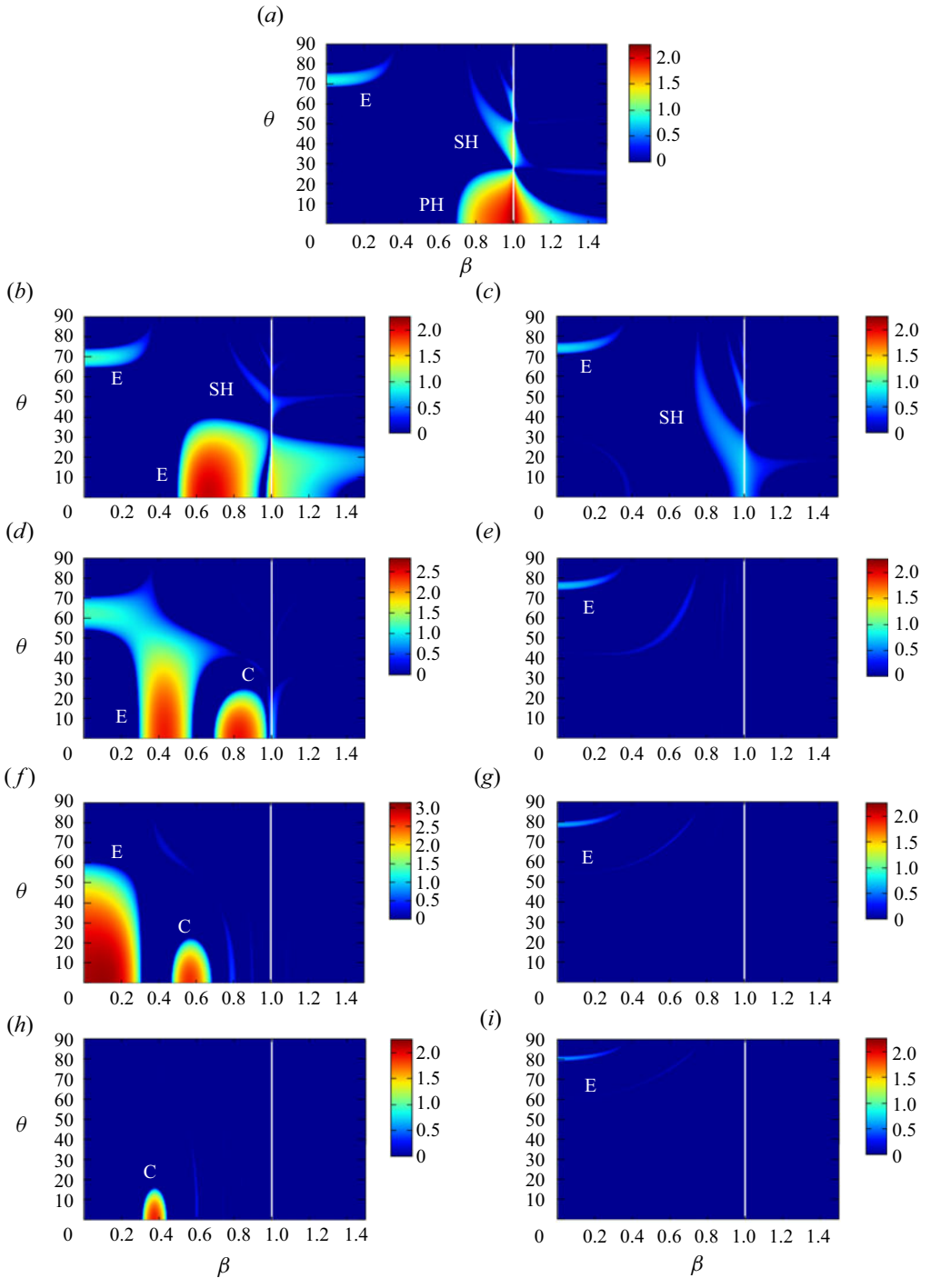

Figure 4. Growth rate $\sigma(\beta, \theta_0, Ro, F_h)$ as a function of β and θ_0 obtained by local stability analysis. Stuart vortices with $C = 1.2$ and $F_h^{-1} = 8$. The Ro^{-1} values are (*a*) 0, (*b*) −2, (*c*) 2, (*d*) −5, (*e*) 5, (*f*) −10, (*g*) 10, (*h*) −15, (*i*) 15.

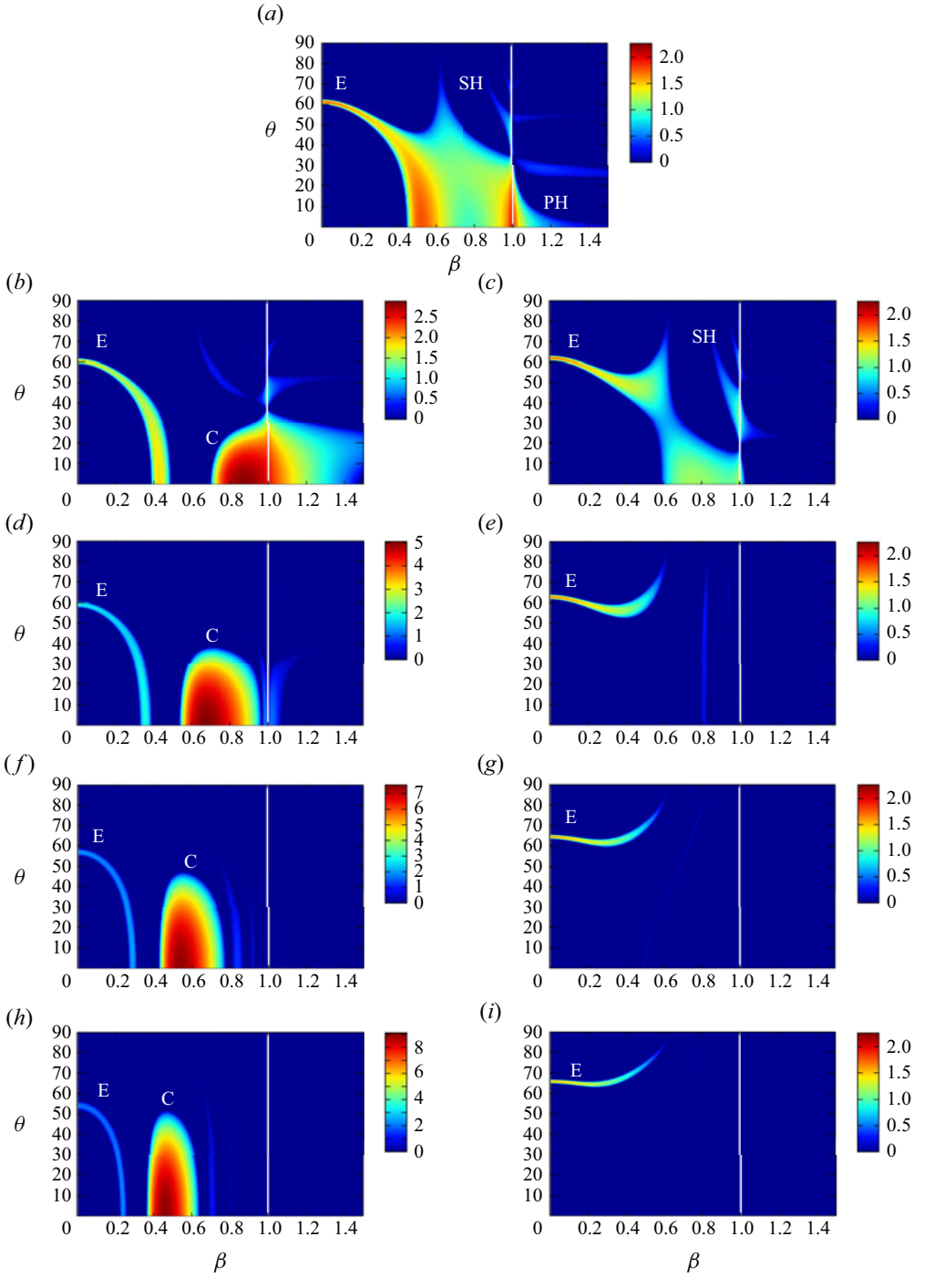

Figure 5. Growth rate $\sigma(\beta, \theta_0, Ro, F_h)$ as a function of β and θ_0 obtained by local stability analysis. Stuart vortices with $C = 2$ and $F_h^{-1} = 8$. The Ro^{-1} values are (*a*) 0, (*b*) −2, (*c*) 2, (*d*) −5, (*e*) 5, (*f*) −10, (*g*) 10, (*h*) −15, (*i*) 15.

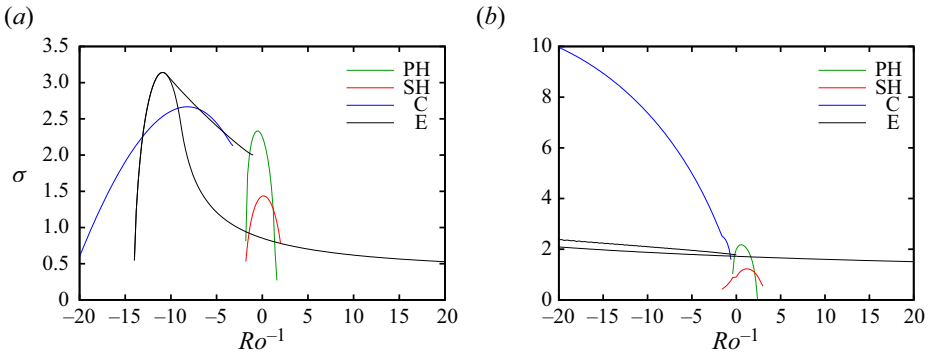

Figure 6. Growth rate $\sigma_{max}(Ro, F_h)$ as a function of Ro obtained by local stability analysis. Here, $F_h^{-1} = 8$ and (*a*) $C = 1.2$, (*b*) $C = 2$.

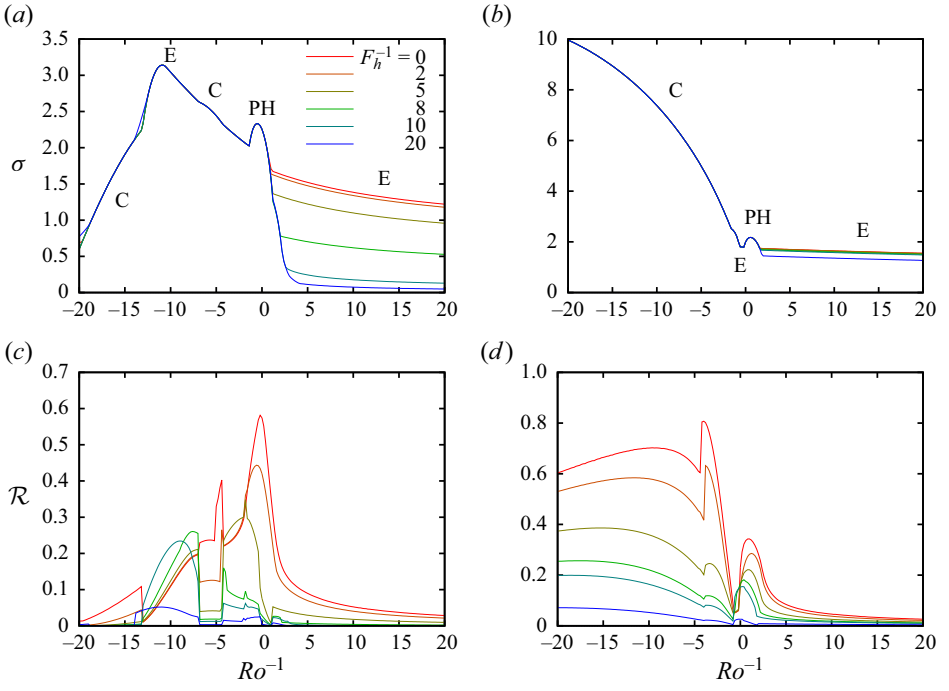

Figure 7. (*a*,*b*) Growth rate $\sigma_{max}(Ro, F_h)$ and (*c*,*d*) realizability $\mathcal{R}$ as a function of Ro obtained by local stability analysis, for (*a*,*c*) $C = 1.2$, (*b*,*d*) $C = 2$.

The dominant instability for $C = 1.2$ changes as follows:

$$\text{for } Ro^{-1} \geqslant 0, \quad PH \;\rightarrow\; (SH \;\rightarrow)\; E, \tag{4.1}$$

$$\text{for } Ro^{-1} \leqslant 0, \quad PH \;\rightarrow\; E \;\rightarrow\; C \;\rightarrow\; E \;\rightarrow\; C, \tag{4.2}$$

as $|Ro^{-1}|$ increases. For $C = 2$, it changes as follows:

$$\text{for } Ro^{-1} \geqslant 0, \quad PH \;\rightarrow\; E, \tag{4.3}$$

$$\text{for } Ro^{-1} \leqslant 0, \quad PH \;\rightarrow\; E \;\rightarrow\; C, \tag{4.4}$$

in the range $|Ro^{-1}| \leqslant 20$.

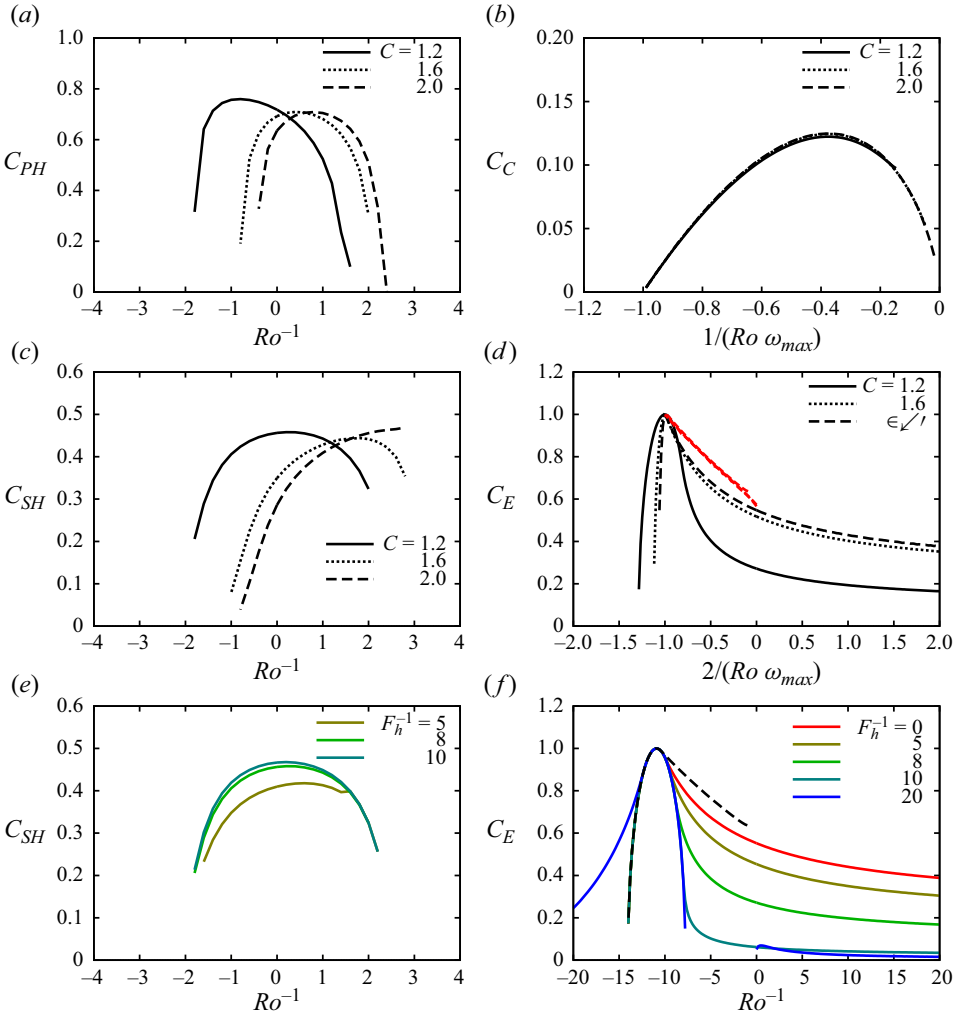

Figure 8. Coefficients that appear in § 2.2 as functions of Ro^{-1} obtained by local stability analysis, where (*a–d*) show C_{PH}, C_C, C_{SH} and C_E, respectively, for $C = 1.2$, 1.6 and 2. In (*c*,*d*), F_h^{-1} is fixed at 8; (*e*,*f*) show C_{SH} and C_E for selected values of F_h^{-1}, while C is fixed at 1.2. The red lines in (*d*) and the dashed line in (*f*) show the branch corresponding to the ring-type elliptic instability that appears for all values of F_h^{-1}.

In order to show the usefulness of the estimates of the growth rate in § 2.2, we evaluate the coefficient of the growth rate introduced in § 2.2 as a function of Ro^{-1} for each instability (figure 8). As in Hattori & Hirota (2023), the coefficients C_{PH} and C_C are compared among $C = 1.2$, 1.6 and 2 as they are independent of stratification (figures 8*a*,*b*). The coefficients C_{SH} and C_E at $F_h^{-1} = 8$ are also compared among $C = 1.2$, 1.6 and 2 (figures 8*c*,*d*), while the effects of stratification are shown at $C = 1.2$ (figures 8*e*,*f*). It is pointed out that the horizontal axis is $1/(Ro\omega_{max})$ and $2/(Ro\omega_{max})$ in figures 8(*b*) and 8(*d*), respectively, to take account of the instability condition for the centrifugal and elliptic instabilities. This figure confirms that the coefficients are $O(1)$ for all instabilities, as in the case of the 2-D Taylor–Green vortices (Hattori & Hirota 2023). Moreover, the coefficient of each instability is comparable in magnitude between the three base

Base flow	C_{PH}	C_C	C_{SH}	C_E
Stuart, $C = 1.2$	0.76	0.12	0.47	1.00
2-D Taylor–Green, $\varepsilon_e/\omega_{max} = 0.2$ (HH2023)	0.90	0.20	0.26	1.00

Table 2. Maximum values of coefficients appearing in estimates of growth rate. Comparison between the Stuart vortices and the 2-D Taylor–Green vortices studied in Hattori & Hirota (2023) (HH2023).

flows; it is smaller for the centrifugal and strato-hyperbolic instabilities than for the pure-hyperbolic and elliptic instabilities. The maximum values of the coefficients shown in table 2 also support this result. It is also pointed out that the curves almost collapse for the centrifugal instability (figure 8*b*), while some differences are observed for the elliptic instability because of the different ratio of F_h^{-1} to ω_{max}. For the elliptic instability, the dependence of the coefficient on the rotation and stratification is also similar to the case of the 2-D Taylor–Green vortices: the maximum is $C_E = 1.0$ at $Ro^{-1} \approx -\omega_{max}/2$; it decreases with stratification for $Ro^{-1} > 0$; for strong stratification $F_h^{-1} = 20 > \omega_{max}/2$, it extends to strong anticyclonic rotation. For the other instabilities, the shapes of the curves are different between the 2-D Taylor–Green vortices and the Stuart vortices; how the coefficients depend on stratification and rotation depends on the vorticity distribution. Thus the estimates of the growth rates in § 2.2 are expected to be generally applicable to various base flows.

4.2. *Results of modal stability analysis*

In this subsection, we show the results of modal stability analysis. Although the numerical domain contains not only the vortex with negative vorticity but also that with positive vorticity, as in the case of the 2-D Taylor–Green vortices (Hattori & Hirota 2023), the distance between the arrays is sufficiently large that the enstrophy of the unstable modes is concentrated in one of the arrays; as a result, the enstrophy ratio ϕ is always close to either 0 or 1 when $Ro^{-1} \neq 0$. Thus we can distinguish between the unstable modes on the cyclonic vortices and those on the anticyclonic vortices when $Ro^{-1} \neq 0$, which is different from the 2-D Taylor–Green vortices. When $Ro^{-1} = 0$, the same modes appear in both arrays. The Floquet exponent is fixed at $\mu = 0$ in this subsection and § 4.3, while it is set to $\mu = 1/2$ in § 4.4 to investigate the properties of the subharmonic modes.

Based on the local stability results, the strength of rotation is chosen from $Ro^{-1} = 0, \pm 5, \pm 10, \pm 15$. The case of no stratification ($F_h^{-1} = 0$) and one case of strong stratification ($F_h^{-1} = 8$) are considered for $C = 1.2$, while the stratified case for $C = 2$ is omitted because it requires higher resolution (Hattori *et al.* 2021); the effects of stratification can be inferred from the results for $C = 1.2$ and the local stability results. The Reynolds number is fixed at $Re = 10^4$. There are non-oscillatory modes as well as oscillatory modes. In the following, all modes for which structures are shown are non-oscillatory (i.e. the complex parts of the eigenvalues are zero) except those shown in figures 12(*b*) and 12(*e*).

4.2.1. *Case $C = 1.2$*

First, we show the results for $C = 1.2$. Figure 9 shows the growth rate $\sigma = \sigma(k_z, Ro, F_h)$ obtained by modal stability analysis in the absence of stratification. The colours of the

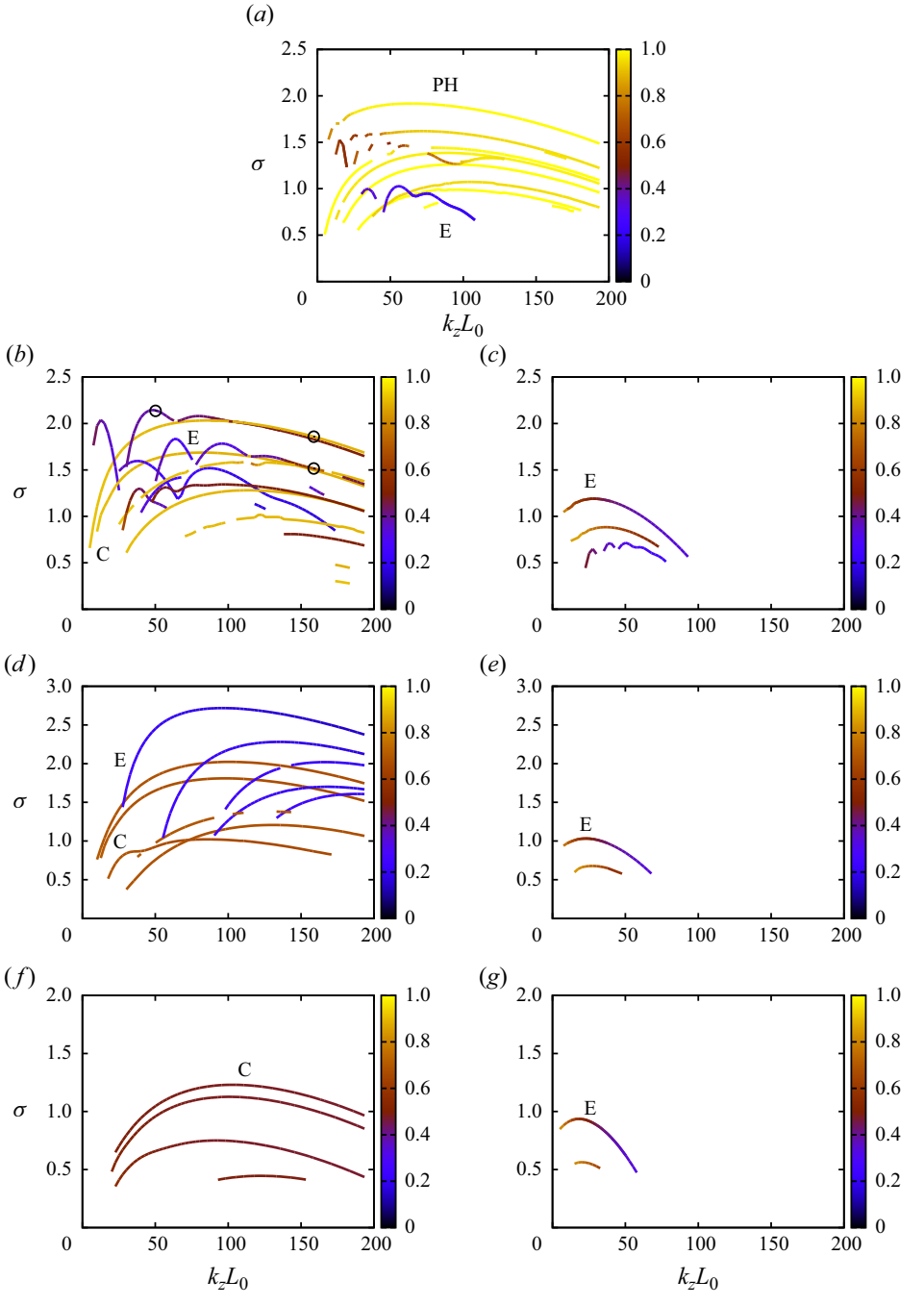

Figure 9. Growth rate $\sigma(k_z, Ro, F_h)$, for $C = 1.2$, $F_h^{-1} = 0$. The Ro^{-1} values are (*a*) 0, (*b*) −5, (*c*) 5, (*d*) −10, (*e*) 10, (*f*) −15, (*g*) 15. The circles in (*b*) correspond to the modes shown in figure 10.

lines show the approximate radius of the mode defined as

$$\bar{\beta} = \frac{\int_{D_\gamma} |\boldsymbol{\omega}'|^2 \beta' \, \mathrm{d}x \, \mathrm{d}y}{\int_{D_\gamma} |\boldsymbol{\omega}'|^2 \, \mathrm{d}x \, \mathrm{d}y}, \tag{4.5}$$

where $\boldsymbol{\omega}' = \boldsymbol{\nabla} \times \boldsymbol{u}'$, D_γ denotes the region that contains the anticyclonic vortex for $\gamma = ac$ and the cyclonic vortex for $\gamma = c$, and β' is the approximate streamline parameter calculated by

$$\beta' = \left(\frac{\Psi - \Psi_e}{\Psi_h - \Psi_e} \right)^{1/2}. \tag{4.6}$$

Here, Ψ_e and Ψ_h are the values of the streamfunction at the elliptic and hyperbolic stagnation points, respectively. The above definition gives the same values for β at the elliptic stagnation point and on the separatrix: $\beta' = 0$ at the elliptic stagnation point, and $\beta' = 1$ on the separatrix. The modes shown by the yellow lines have large amplitudes near the separatrix, while those shown by the blue lines are concentrated near the elliptic stagnation point.

For $Ro^{-1} = 0$ (figure 9*a*), most of the modes are due to the pure-hyperbolic instability, while some modes of the elliptic instability with small $\bar{\beta}$ are observed; there are also mixed-type modes of the pure-hyperbolic and elliptic instabilities at low wavenumbers (Hattori *et al.* 2021). For $Ro^{-1} = -5$ (figure 9*b*), the modes with large $\bar{\beta}$ shown by the yellow lines correspond to the centrifugal instability; an example of the mode structures is shown in figure 10(*a*). On the other hand, the modes with small $\bar{\beta}$ shown by the blue lines, which form peaks at low wavenumbers, and the brown lines, which extend to high wavenumbers, correspond to the elliptic instability; examples of the mode structures are shown for a peak at $k_z L_0 = 50.3$ in figure 10(*b*) and a high wavenumber at $k_z L_0 = 158.3$ in figure 10(*c*). The maximum growth rate of the elliptic instability mode is 2.14, which is larger than that for $Ro^{-1} = 0$. For $Ro^{-1} = -10$ (figure 9*d*), the values of the approximate radius $\bar{\beta}$ of the centrifugal instability modes decrease to approximately 0.6 (shown by the brown lines) as predicted by local stability analysis. The narrow peaks of the elliptic instability disappear. However, the branches with small $\bar{\beta}$ shown by the blue lines are due to the elliptic instability. The maximum growth rate of the centrifugal instability is 2.02, which is close 2.03 for $Ro^{-1} = -5$, while the maximum growth rate of the elliptic instability is 2.72, which is larger than 2.14 for $Ro^{-1} = -5$. For $Ro^{-1} = -15$ (figure 9*f*), only the centrifugal instability survives with reduced growth rate. For $Ro^{-1} > 0$ (figures 9*c*,*e*,*g*), a few branches at low wavenumbers, which correspond to the elliptic instability, are found for each case.

The types of instability observed for each value of Ro^{-1} and the growth rates are in reasonable agreement with the local stability results. The pure-hyperbolic, elliptic and centrifugal instabilities are observed, while the strato-hyperbolic instability is not observed. The maximum growth rate of the elliptic instability at $Ro^{-1} = -10$ is $\sigma \approx 2.72$, which is slightly smaller than 3.04 obtained by local stability analysis; this is due to viscous effects as shown in § 4.3. The approximate radius of the centrifugal instability and elliptic instability decreases with the magnitude of rotation for $Ro^{-1} < 0$. The elliptic instability is stabilized for $Ro^{-1} = -15$, which satisfies $-3\omega_{max}/2 < Ro^{-1} < -\omega_{max}/2$ (§ 2.2). Only the elliptic instability survives for $Ro^{-1} \geqslant 5$.

Figure 11 shows the growth rate $\sigma = \sigma(k_z, Ro, F_h)$ for a stratified case ($F_h^{-1} = 8$). The cyclonic cases ($Ro^{-1} > 0$) are omitted because no branch was found for $Ro^{-1} \geqslant 5$. For $Ro^{-1} = 0$ (figure 11*a*), all modes except those shown by the blue line, which is due to the elliptic instability, are the pure-hyperbolic instability modes. For $Ro^{-1} = -5$ (figure 11*b*), the branches with $\bar{\beta} \lesssim 0.6$ (brown lines and blue lines) are due to the elliptic instability, while those with $\bar{\beta}$ close to 1 (yellow lines) are the centrifugal instability modes. The maximum growth rate of the elliptic instability modes is $\sigma = 1.81$, which is larger than

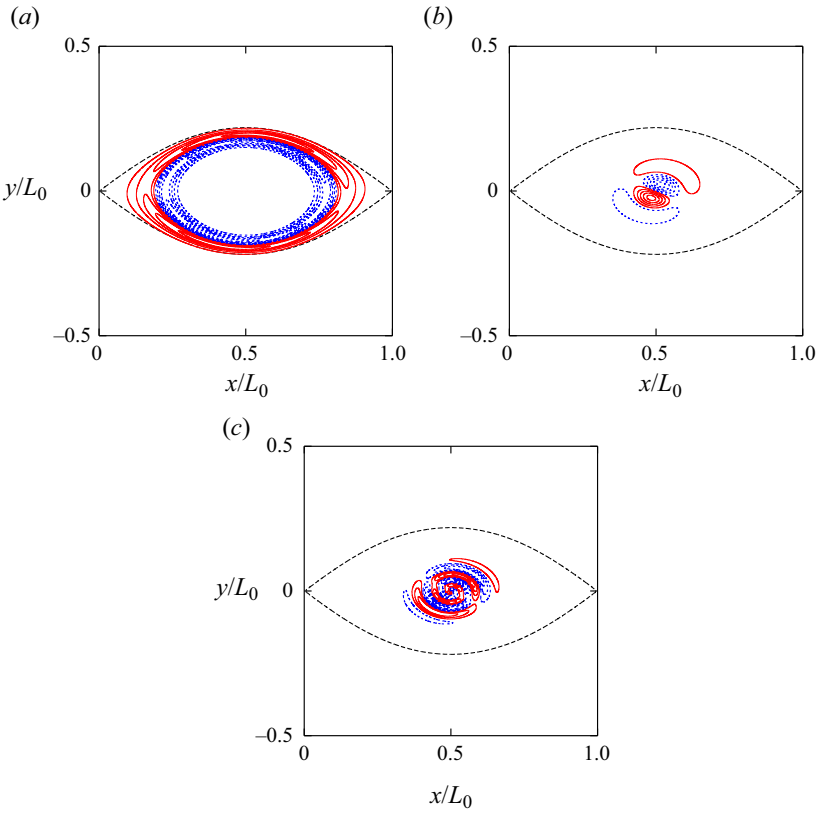

Figure 10. Mode structures shown by contours of ω_z' on the (x, y) plane, for $C = 1.2$, $F_h^{-1} = 0$ and $Ro^{-1} = -5$. The contours of ω_z' are drawn for $|\omega_z'|/|\omega_z'|_{max} = 0.1, 0.3, 0.5, 0.7, 0.9$; the red and blue lines correspond to positive and negative values, respectively. (*a*) Centrifugal instability mode with $k_z L_0 = 158.3$, $\sigma = 1.86$ and $\bar{\beta} = 0.885$. (*b*) Elliptic instability mode with $k_z L_0 = 50.3$, $\sigma = 2.14$ and $\bar{\beta} = 0.377$. (*c*) Elliptic instability mode with $k_z L_0 = 158.3$, $\sigma = 1.52$ and $\bar{\beta} = 0.640$.

$\sigma = 1.34$ of the centrifugal instability modes. It is pointed out that the elliptic instability is divided into two types: a ring-type elliptic (rE) instability mode (figures 12*a*,*b*) with $\bar{\beta} \approx 0.5$ shown by the brown lines in figure 11(*b*), which corresponds to the unstable region attached to $\theta_0 = 0^\circ$ in the local stability analysis, and a usual mode with $\bar{\beta} \lesssim 0.4$ shown by the blue lines in figure 11(*b*), which appears near the elliptic stagnation point (figure 12*c*). We also point out that the azimuthal wavenumbers of the inertial waves composing the ring-type elliptic instability modes in figures 12(*a*) and 12(*b*) are different: $(m, m+2) = (-1, 1)$ in figure 12(*a*), while $(m, m+2) = (0, 2)$ for the oscillating mode shown in figure 12(*b*). The centrifugal instability modes shown in figures 12(*d*) and 12(*e*) have large amplitude near the separatrix in accordance with local stability results. It is also pointed out that the radius of the ring-type mode of the elliptic instability (figures 12*a*,*b*) is different from that of the centrifugal instability mode (figure 12*d*) for the same values of F_h^{-1} and Ro^{-1}, which confirms that their instability mechanisms are different (see also § 4.3 for further confirmation). The centrifugal instability mode shown in figure 12(*d*) is symmetric and non-oscillatory, while that shown in figure 12(*e*) is antisymmetric and oscillatory; the azimuthal wavenumbers of these modes are 0 and 1, respectively. Although the two branches of the centrifugal instability have nearly same maximum growth rates at

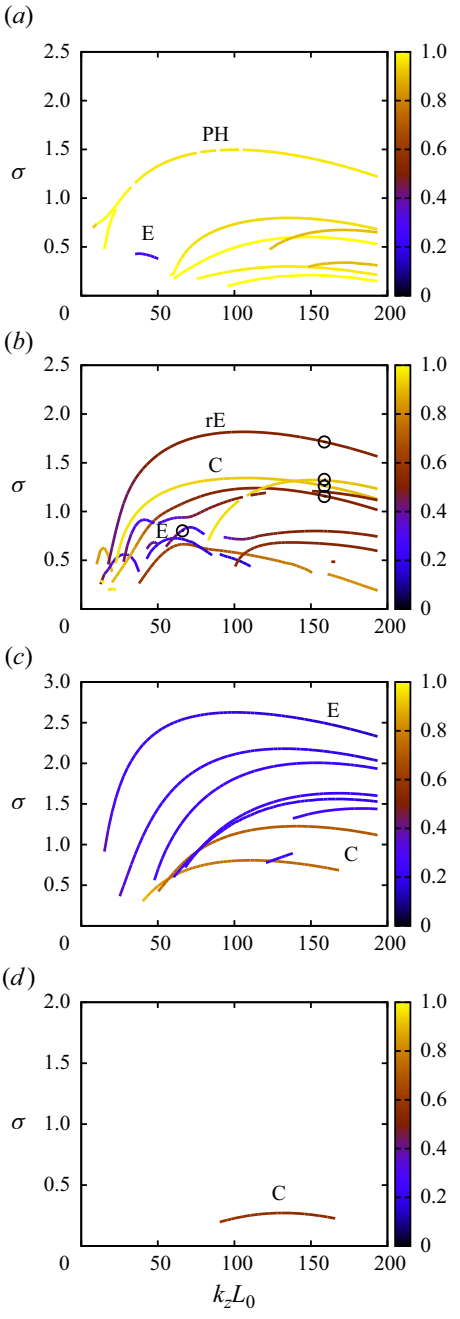

Figure 11. Growth rate $\sigma(k_z, Ro, F_h)$, for $C = 1.2$, $F_h^{-1} = 8$. The Ro^{-1} values are (*a*) 0, (*b*) −5, (*c*) −10, (*d*) −15. The circles in (*b*) correspond to the modes shown in figure 12.

$Ro^{-1} = -5$, the antisymmetric oscillatory branch has larger growth rate than the symmetric non-oscillatory branch at stronger rotation $Ro^{-1} = -10$. The antisymmetric oscillatory mode can be dominant at finite Reynolds number in non-rotating stratified fluids (Yim & Billant 2016).

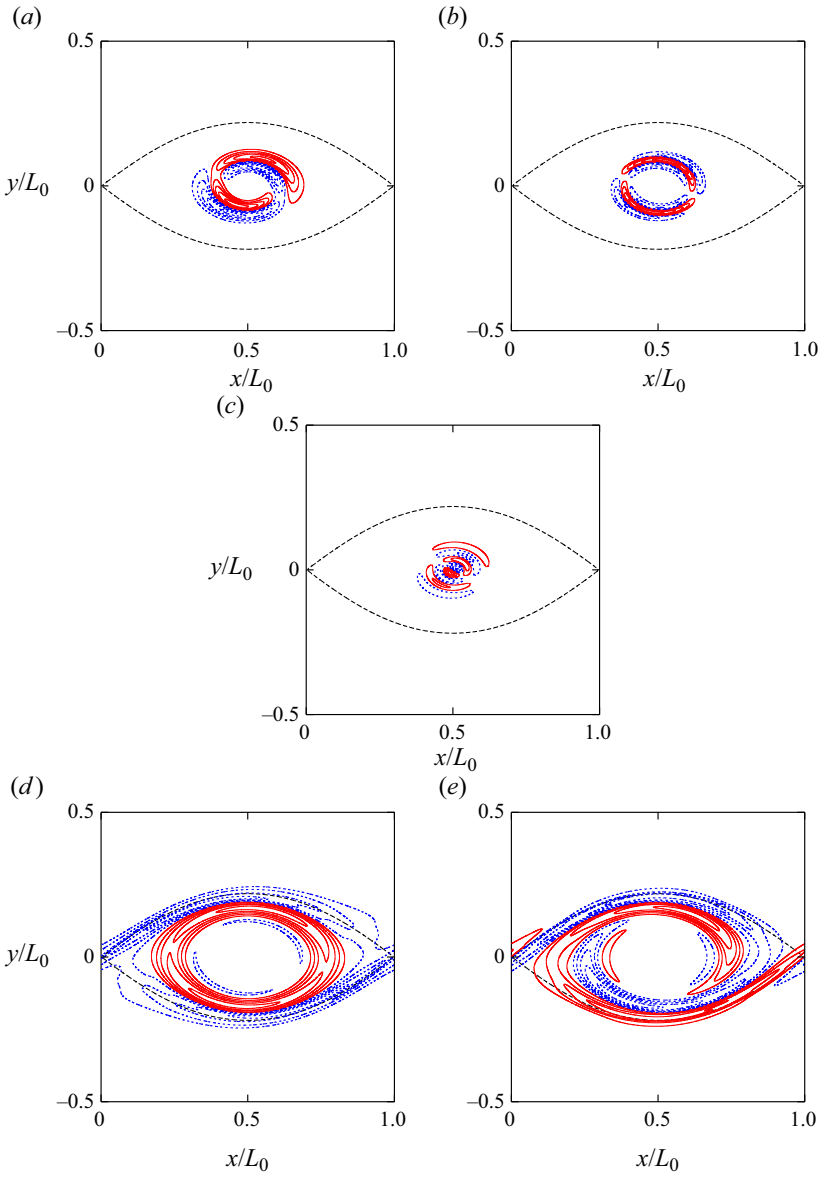

Figure 12. Mode structures shown by contours of ω_z' on the (x, y) plane, for $C = 1.2$, $F_h^{-1} = 8$ and $Ro^{-1} = -5$. The contours of ω_z' are drawn as in figure 10. (*a*) Ring-type elliptic instability mode with $k_z L_0 = 158.3$, $\sigma = 1.72$ and $\bar{\beta} = 0.517$. (*b*) Oscillating ring-type elliptic instability mode with $k_z L_0 = 158.3$, $\sigma = 1.16$, $\omega = 7.26$ and $\bar{\beta} = 0.517$. (*c*) Elliptic instability mode with $k_z L_0 = 62.8$, $\sigma = 0.768$ and $\bar{\beta} = 0.400$. (*d*) Centrifugal instability mode with $k_z L_0 = 158.3$, $\sigma = 1.32$ and $\bar{\beta} = 0.915$. (*e*) Oscillating centrifugal instability mode with $k_z L_0 = 158.3$, $\sigma = 1.27$, $\omega = 3.24$ and $\bar{\beta} = 0.907$. For the oscillating modes, the frequency ω is also given.

For $Ro^{-1} = -10$ (figure 11*c*), the growth rate of the elliptic instability modes, for which $\beta \lesssim 0.3$ (blue lines), becomes large, with the maximum growth rate being $\sigma = 2.63$, while the growth rate of the centrifugal instability is $\sigma = 1.23$, which is slightly smaller than that for $Ro^{-1} = -5$. The maximum growth rate will be compared to those obtained by the

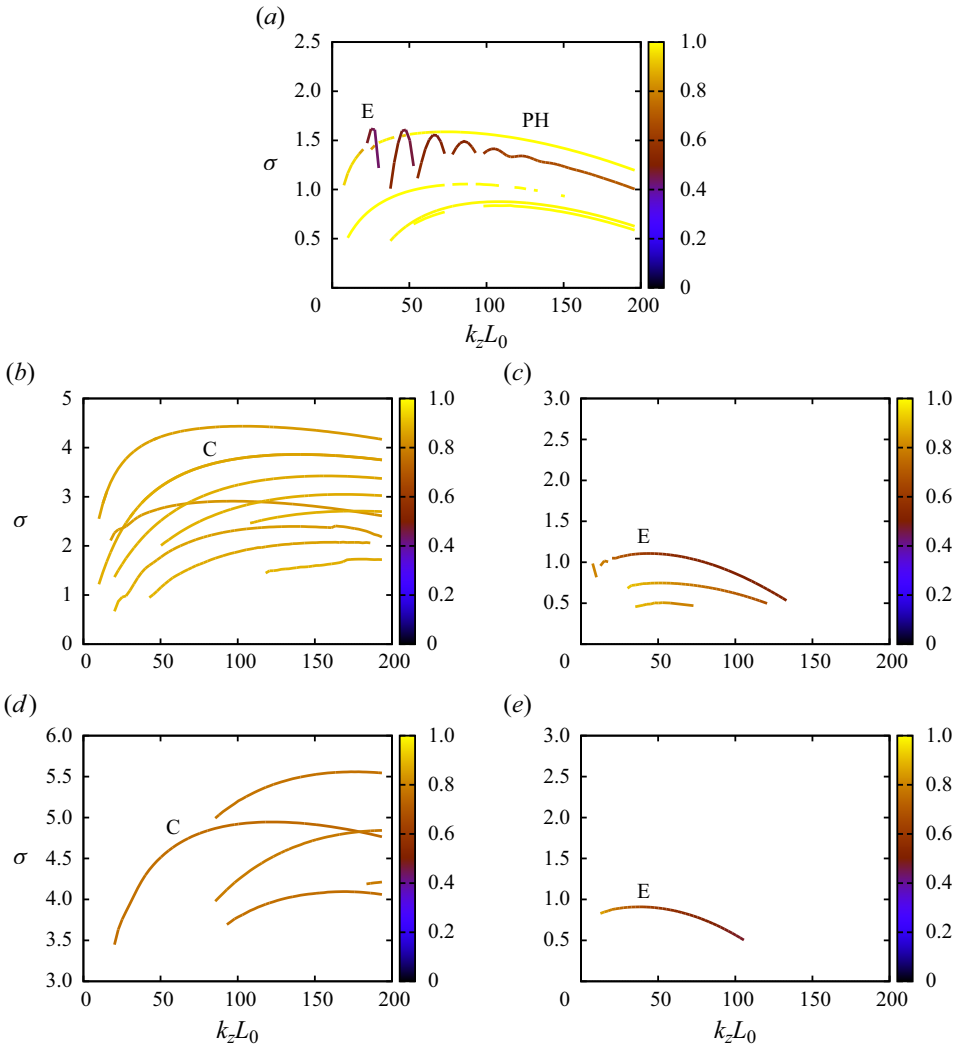

Figure 13. Growth rate $\sigma(k_z, Ro, F_h)$, for $C = 2$, $F_h^{-1} = 0$. The Ro^{-1} values are (*a*) 0, (*b*) −5, (*c*) +5, (*d*) −10, (*e*) +10.

local stability analysis in § 4.3. For $Ro^{-1} = -15$ (figure 11*d*), only one weak branch of the centrifugal instability is observed.

4.2.2. *Case C = 2*

Next, we show the results for $C = 2$. Figure 13 shows the growth rate $\sigma = \sigma(k_z, Ro, F_h)$ plotted against the wavenumber k_z for the non-stratified case ($F_h^{-1} = 0$). As in the case $C = 1.2$, the pure-hyperbolic instability modes with $\bar{\beta}$ close to 1 (yellow lines) and the elliptic instability modes with $\bar{\beta} \lesssim 0.5$ (brown lines) are observed for $Ro^{-1} = 0$. For $Ro^{-1} = -5$ and -10, only the centrifugal instability modes are observed (figure 14); this is in accordance with the local stability results as the growth rate of the centrifugal instability is much larger than those of the other instabilities for $C = 2$. The maximum growth rate

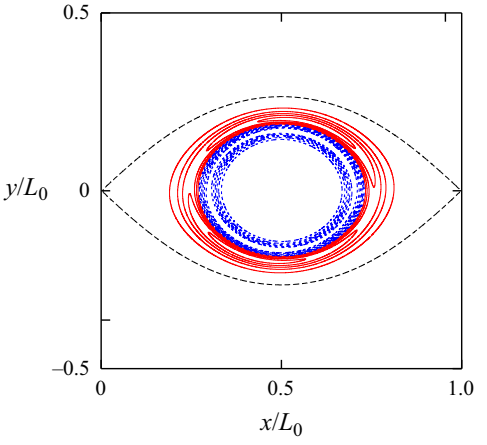

Figure 14. Mode structures shown by contours of ω_z' on the (x, y) plane, for $C = 2$, $F_h^{-1} = 0$ and $Ro^{-1} = -5$. The contours of ω_z' are drawn as in figure 10. Centrifugal instability mode with $k_z L_0 = 158.3$, $\sigma = 4.32$ and $\tilde{\beta} = 0.842$.

is $\sigma = 4.44$ and 5.56 for $Ro^{-1} = -5$ and -10, respectively, which are smaller than the values 4.99 and 7.38 predicted by the local stability analysis because of the viscous effects.

For $Ro^{-1} = 5$ and 10, a few branches of the elliptic instability are observed. The growth rates are close to those for $C = 1.2$ as predicted by local stability analysis, while the branches extend to high wavenumbers because the core size of the Stuart vortices is smaller for $C = 2$, as shown in figure 1(*c*).

The effects of stratification can be inferred from the results for $C = 1.2$, although the stratified case is omitted for $C = 2$. The growth rate of the centrifugal instability will decrease with the strength of stratification. Then the ring-type elliptic instability modes can be captured depending on the strength of rotation, while the normal elliptic instability modes will disappear for strong stratification.

4.3. *Comparison between local and modal stability analysis*

In this subsection, we compare the local stability results and the modal stability results. Direct correspondence between the local and modal stability analysis has been established in Suzuki *et al.* (2018), Hattori *et al.* (2021) and Hattori & Hirota (2023) for the 2-D Taylor–Green vortices. It would give a firm physical origin of the unstable modes also for the Stuart vortices because the mechanism of the instability is clear in the local stability analysis; it will further support the usefulness of the local stability analysis.

Figure 15 compares the structures of unstable modes to the corresponding solutions to the local stability equations for three modes shown in figure 12: the ring-type elliptic instability mode with $k_z L_0 = 158.3$, $\sigma = 1.72$ and $\beta = 0.48$, the elliptic instability mode with $k_z L_0 = 62.8$, $\sigma = 0.768$ and $\beta = 0.80$, and the centrifugal instability mode with $k_z L_0 = 158.3$, $\sigma = 1.32$ and $\beta = 0.05$, where $C = 1.2$, $F_h^{-1} = 8$ and $Ro^{-1} = -5$. As in Hattori & Hirota (2023), the horizontal divergence $\boldsymbol{\nabla}_h \cdot \boldsymbol{u}_h' = \partial u'/\partial x + \partial v'/\partial y$, the vertical component of vorticity ω_z' and the density ρ' of the unstable mode on a streamline of nearly largest amplitude of ω_z' are plotted against time of fluid particle motion that is dictated by (2.12) (figures 15*a*,*c*,*e*); the corresponding variables p, q and s defined by (2.16*a–c*) of the solution to the local stability equations on the same streamline are shown

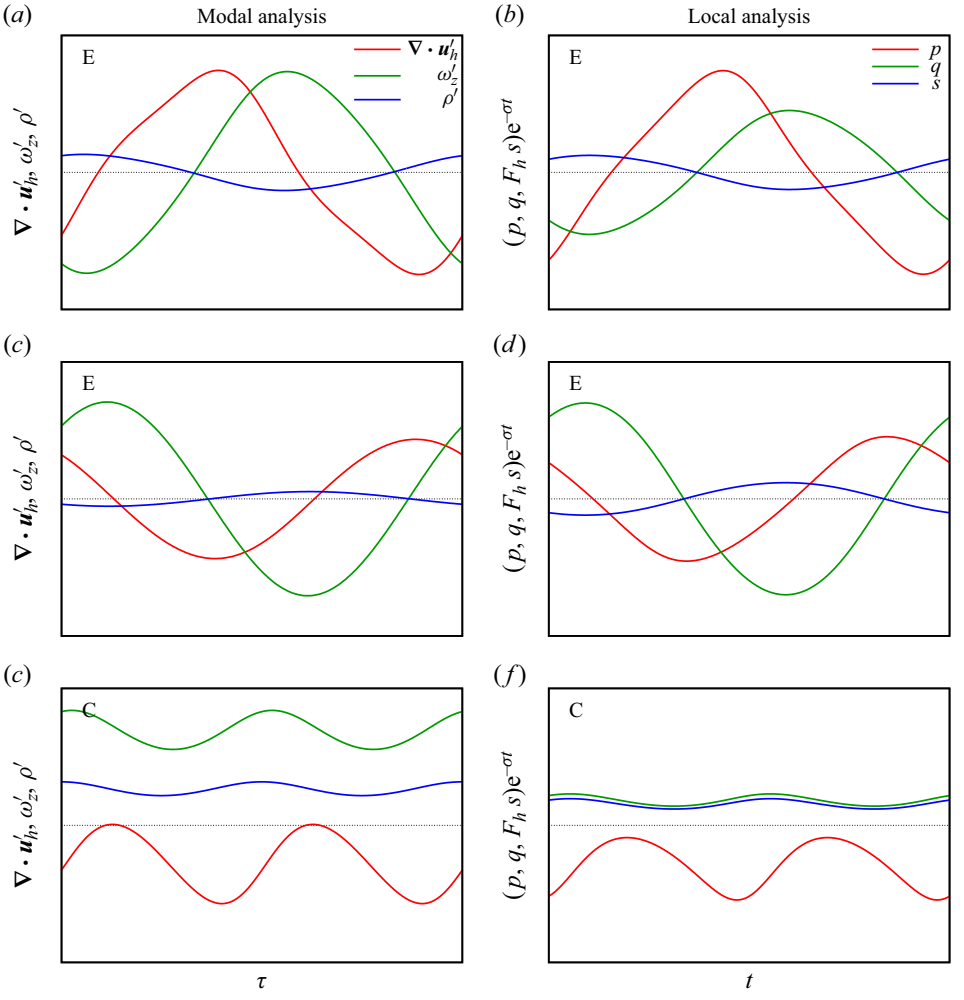

Figure 15. Comparison between modal and local stability analysis, for $C = 1.2$, $F_h^{-1} = 8$ and $Ro^{-1} = -5$. (*a*,*c*,*e*) The values of $\nabla_h \cdot \boldsymbol{u}_h' = \partial u'/\partial x + \partial v'/\partial y$, ω_z' and ρ' of the unstable eigenmode obtained by modal stability analysis are shown as functions of time of a fluid particle on the streamline where ω_z' is maximum. (*b*,*d*,*f*) The corresponding values of p, q and s on the same streamline are multiplied by $\mathrm{e}^{-\sigma t}$ to compensate the exponential growth. (*a*,*b*) Ring-type elliptic instability mode with $k_z L_0 = 158.3$, $\sigma = 1.72$ and $\beta = 0.48$. (*c*,*d*) Elliptic instability mode with $k_z L_0 = 62.8$, $\sigma = 0.768$ and $\beta = 0.80$. (*e*,*f*) Centrifugal instability mode with $k_z L_0 = 158.3$, $\sigma = 1.32$ and $\beta = 0.05$.

in figures 15(*b*), 15(*d*) and 15(*f*), where the values are multiplied by $\mathrm{e}^{-\sigma t}$ to compensate the exponential growth. We observe good agreement between the modal and local results, while there are some differences in magnitude for the centrifugal instability mode. The characteristics of each mode are similar to those of the 2-D Taylor–Green vortices; the phase change is 2π for the elliptic instability, while the variables do not change their signs for the centrifugal instability mode. In addition, the structures of the ring-type elliptic instability are similar to those of the elliptic instability; this confirms the nature of the ring-type elliptic instability, while they are apparently different in figure 12.

Figure 16 compares the growth rates obtained by the local and modal stability analysis for $F_h^{-1} = 0$ and $F_h^{-1} = 8$, with C being fixed at 1.2; the growth rate $\sigma_{max}(Ro, F_h)$ obtained

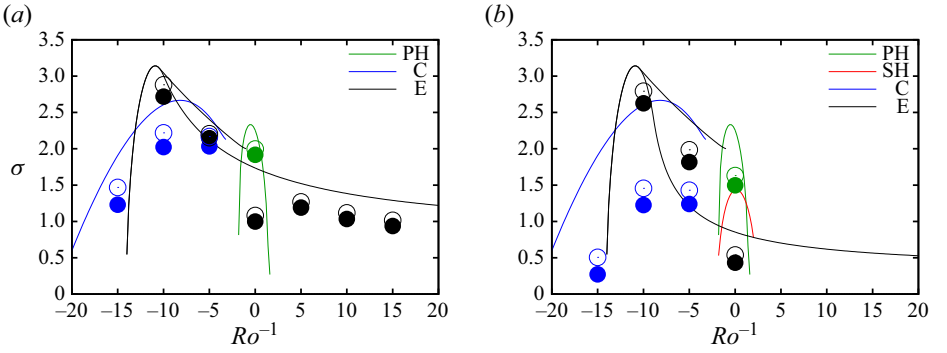

Figure 16. Growth rate $\sigma_{max}(Ro, F_h)$ as a function of Ro. Comparison between local stability analysis (lines) and modal stability analysis (solid circles); the growth rate for the inviscid case is also estimated by subtracting the viscous contribution for the modal stability analysis (open circles). Here, $C = 1.2$ and (*a*) $F_h^{-1} = 0$, (*b*) $F_h^{-1} = 8$.

by local stability analysis is shown by lines as a function of Ro^{-1} for each instability, while the maximum growth rate obtained by modal stability analysis is shown for selected values of Ro^{-1} by solid circles. For the latter, the corrected growth rate in the absence of viscous effects was also estimated by subtracting the viscous contribution as

$$\sigma_{inv} = \sigma - \frac{1}{Re}\frac{\displaystyle\int \boldsymbol{u}' \cdot \nabla^2 \boldsymbol{u}' \,\mathrm{d}x\,\mathrm{d}y\,\mathrm{d}z}{\displaystyle\int |\boldsymbol{u}'|^2 \,\mathrm{d}x\,\mathrm{d}y\,\mathrm{d}z}, \tag{4.7}$$

and is included as open circles. For $F_h^{-1} = 0$, the modal stability growth rates are slightly smaller than $\sigma_{max}(Ro, F_h)$; this is reasonable since the modal stability growth rate cannot exceed the local stability results. For $F_h^{-1} = 8$, however, the difference between the modal and local growth rates depends on the type of instability; it is similar to the case of $F_h^{-1} = 0$ for the elliptic instability, while the difference is larger than $F_h^{-1} = 0$ for the centrifugal instability. For example, the ratios of the corrected modal growth rate to the local growth rate at $Ro^{-1} = -10$ are 92 % and 56 % for the elliptic instability and the centrifugal instability, respectively. This difference is understood in terms of the realizability. As shown in figure 7, the realizability of the centrifugal instability, which is the dominant instability for $Ro^{-1} < -13.2$ and $-6.8 < Ro^{-1} < -4.4$, decreases significantly with F_h^{-1}, while it does not change very much for the elliptic instability, which is dominant for $-13.2 < Ro^{-1} < -6.8$. The significantly reduced realizability corresponds to the narrow range of θ_0 in the unstable region on the (β, θ_0) plane; then an eigenmode constructed at a finite wavenumber should include an area of small growth rate on the (β, θ_0) plane, leading to the reduced growth rate.

4.4. *Subharmonic modes*

So far, we have been concerned with disturbances that have the same spatial period as the base flow in the x direction, which are sometimes called fundamental modes. In this subsection, we investigate the properties of the subharmonic modes by setting the Floquet exponent in (3.5) to $\mathrm{i}\mu = \mathrm{i}/2$. The base flow parameter is fixed at $C = 1.2$.

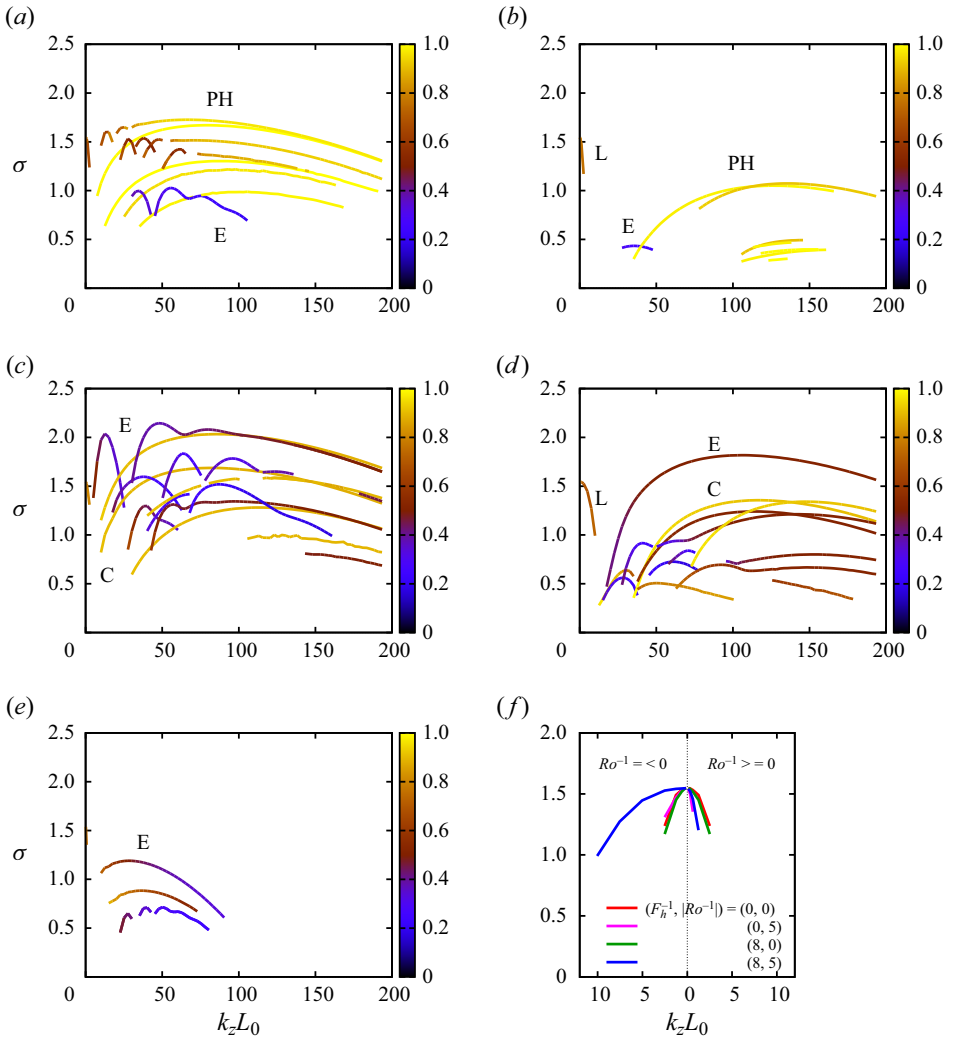

Figure 17. Growth rate $\sigma(k_z, Ro, F_h)$ for subharmonic modes, $C = 1.2$. The (F_h^{-1}, Ro^{-1}) values are (*a*) (0, 0), (*b*) (8, 0), (*c*) (0, −5), (*d*) (8, −5), (*e*) (0, +5). The low-wavenumber modes are compared in (*f*).

Figure 17 shows the growth rate of the subharmonic modes for $(F_h^{-1}, Ro^{-1}) = (0, 0)$, (8, 0), (0, −5), (8, −5), (0, +5). There are two important differences from the case $\mu = 0$.

First, long-wave modes marked by L appear near $k_zL_0 = 0$ for all cases; the growth rates are compared in figure 17(*f*), including an additional case $(F_h^{-1}, Ro^{-1}) = (8, +5)$. the maximum growth rate at $k_zL_0 = 0$ is nearly the same for all cases. The bandwidth of the unstable wavenumber decreases for cyclonic rotation, while it increases for the anticyclonic case with stratification. The corresponding unstable modes with $k_zL_0 = 0.1$ shown in figure 18 are pairing modes that displace the vortex in the direction $x = y$, while the neighbouring vortex is displaced in the opposite direction (Pierrehumbert & Widnall 1982); the mode for $(F_h^{-1}, Ro^{-1}) = (0, 0)$ (figure 18*a*) is nearly identical to that for $(F_h^{-1}, Ro^{-1}) = (8, -5)$ (figure 18*b*), showing that the mode structure does not depend very much on the stratification and rotation.

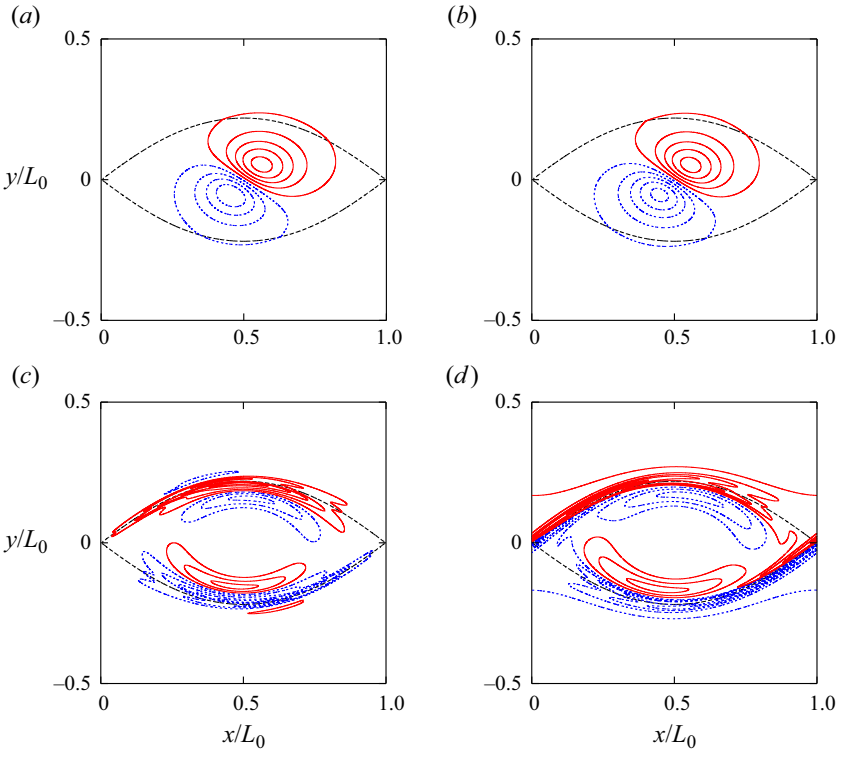

Figure 18. Mode structures shown by contours of ω_z' on the (x, y) plane, for $C = 1.2$. (*a*,*b*) The subharmonic modes of long-wave instability with $k_z L_0 = 0.1$ are compared between (*a*) $(F_h^{-1}, Ro^{-1}) = (0, 0)$ and (*b*) $(8, -5)$. (*c*) The subharmonic mode ($\mu = 1/2$) and (*d*) the fundamental mode ($\mu = 0$) of pure-hyperbolic instability with $k_z L_0 = 158.3$ are compared. The contours of ω_z' are drawn as in figure 10.

Second, the growth rates of the pure-hyperbolic instability modes are smaller than the case $\mu = 0$; the maximum growth rates at $(F_h^{-1}, Ro^{-1}) = (0, 0)$ and $(8, 0)$ are 1.73 and 1.07, respectively, for $\mu = 1/2$, while they are 1.92 and 1.50 for $\mu = 0$. This smaller growth rate of the subharmonic mode can be understood by the mode structures shown in figure 18(*c*). The mode has small amplitudes near the hyperbolic stagnation points to match the reversed phase in the neighbouring regions, while the corresponding mode for $\mu = 0$ has large amplitudes there. As a result, the effects of strain near the hyperbolic stagnation points are weaker for the subharmonic modes, leading to smaller growth rates.

Besides the above two differences, however, the growth rates of the subharmonic modes are nearly the same as those of the fundamental modes; this is because the centrifugal instability modes and the elliptic instability modes are contained inside the separatrix so that the mode structures are unaffected by the matching condition for the phase at the hyperbolic stagnation points. The subharmonic pairing instability mode is dominant for strong cyclonic rotation or strong stratification without rotation, while the pure-hyperbolic, elliptic and centrifugal instability modes are dominant in the other cases.

4.5. *Comparison to previous works on Stuart vortices*

Here, we compare the present results with previous works on the stability of the Stuart vortices. Table 3 lists previous works that investigated the effects of rotation on the stability

Work	Method	ρ_s	Range of Ro^{-1}
Pierrehumbert & Widnall (1982)	Modal	[0, 0.3]	0
Leblanc & Cambon (1998)	Local/modal	0, 0.1, 0.2, 0.33	[−12.6, 6.3]
Potylitsin & Peltier (1999)	Modal	0.33, 0.75	[−0.5, 0.1]
Godeferd *et al.* (2001)	Local	0.33, 0.75, 0.90	[−22, 0]
Present	Local/modal	0.55, 0.78, 0.87	[−20, 20]

Table 3. Previous works on stability of Stuart vortices. Comparison of the method of stability analysis, the parameter ρ_s for the Stuart vortices and the range of the Rossby number.

of the Stuart vortices, while a pioneering work, Pierrehumbert & Widnall (1982), without rotation is also included. In this table, the values of the Rossby number were converted taking account of the difference in the definition. It is pointed out that the range of the Rossby number is limited to weak rotation in the modal stability analysis, although Leblanc & Cambon (1998) considered strong rotation up to $Ro^{-1} = -12.6$. Also, the results in the previous works are rather limited. In Potylitsin & Peltier (1999), the results are shown for only two values of the wavenumber ($k_z = 2$ and 3) with weak rotation. In Leblanc & Cambon (1998), the structure of the fundamental modes is shown only for the elliptic instability at $k_z = 2$; they could not find the centrifugal instability mode or the pure-hyperbolic instability mode by modal stability analysis, although they were discussed by local stability analysis. In this regard, the present work has explored much broader aspects of the instability of the Stuart vortices by (i) showing the growth rate as a function of wavenumber up to large values of k_z, (ii) investigating the effects of strong rotation as well as weak rotation, and (iii) clarifying the effects of stratification.

The magnitude of the growth rate is compared between the present work and the previous works; here, we should take account of the different scaling. The growth rates of the pairing instability, the pure-hyperbolic instability, the elliptic instability and the centrifugal instability obtained in the previous modal stability results (Pierrehumbert & Widnall 1982; Leblanc & Cambon 1998; Potylitsin & Peltier 1999) under the present scaling are typically $\sigma \sim 0.3 \times L_0/U_0 \approx 1.9$ without rotation, while they can be $\sigma \sim 0.5 \times L_0/U_0 \approx 3.1$ with rotation. These are close to the growth rates obtained for $C = 1.2$ or $\rho_s = 0.55$ in the present study. The maximum growth rate of the centrifugal instability obtained by local stability analysis of Godeferd *et al.* (2001) was $\sigma \sim 0.8 \times L_0/U_0 \approx 5.0$ for $\rho_s = 0.75$; this is close to $\sigma = 6.1$ for $C = 1.6$ or $\rho_s = 0.78$ in the present study.

5. Concluding remarks

The linear stability of the Stuart vortices in rotating stratified fluids has been studied by local and modal stability analysis. As in the case of the 2-D Taylor–Green vortices (Hattori & Hirota 2023), five types of instability are identified by local stability analysis: the pure-hyperbolic instability, the strato-hyperbolic instability, the rotational-hyperbolic instability, the centrifugal instability and the elliptic instability. The effects of stratification and rotation on each instability were investigated in detail. The pure-hyperbolic instability is dominant only when both rotation and stratification are weak. For strong anticyclonic rotation, the elliptic instability or the centrifugal instability becomes dominant depending on $\varepsilon_e/\omega_{max}$, the ratio of the strain rate and the vorticity at the elliptic stagnation point, and the magnitude of rotation; further stronger rotation stabilizes both instabilities.

For strong cyclonic rotation, the elliptic instability becomes dominant, although the growth rate is smaller than the anticyclonic cases. Most of these results were confirmed by modal stability analysis, although there are a few differences: unstable modes of the strato-hyperbolic instability and the rotational-hyperbolic instability were not found because their growth rates and the realizability are smaller than for the other instabilities; when stratification is strong, the growth rate of the centrifugal instability modes is smaller than that predicted by local stability analysis. The effects of stratification on the subharmonic modes were also investigated. The maximum growth rate at $k_z = 0$ does not differ very much between the non-stratified case $F_h^{-1} = 0$ and the stratified case $F_h^{-1} = 8$; the range of the unstable wavenumber decreases for cyclonic rotation, while it increases for the anticyclonic case with stratification. The zigzag and radiative instability were not found in the present work. According to Billant *et al.* (2010), the zigzag instability occurs for a counter-rotating vortex pair, but does not for a co-rotating vortex pair. Thus it will not occur for the Stuart vortices. It may not be easy to find the radiative instability in the present case because it is not a strong instability (Park & Billant 2013).

We emphasize that the condition and the estimate of the growth rate of each instability summarized by Hattori & Hirota (2023) are useful not only for the 2-D Taylor–Green vortices (Hattori & Hirota 2023) but also for the Stuart vortices. In fact, the magnitudes of the coefficients that appear in the estimates in § 2.2 are similar to those for the 2-D Taylor–Green vortices (Hattori & Hirota 2023); in addition, the coefficients depend on rotation and stratification in a similar way for the two different base flows. Therefore, the conditions and the estimates of the growth rates would serve as useful sources of information for the instability of vortices in rotating stratified fluids in general; they can be used to predict which instability is dominant once the values of the strain rates and the maximum vorticity are available. In fact, the differences between the 2-D Taylor–Green vortices and the Stuart vortices are understood by the differences of these values characterizing the vorticity distribution: the ratio of the strain rates $\varepsilon_e/\varepsilon_h$ is larger for the Stuart vortices than for the 2-D Taylor–Green vortices, which explains why the elliptic instability is more dominant than the hyperbolic instabilities for the Stuart vortices; the ratios of the strain rates to the maximum vorticity $\varepsilon_h/\omega_{max}$ and $\varepsilon_e/\omega_{max}$ are smaller for the Stuart vortices, which explains why the centrifugal instability becomes dominant in wide ranges of parameters. It is also pointed out that the local stability analysis further proved valuable as direct correspondence between the local unstable solutions and the unstable eigenmodes has been established also for the Stuart vortices; however, this does not apply to the subharmonic modes caused by global pairing.

Another important contribution of the present work is the discovery of the ring-type modes of the elliptic instability. The ring-type elliptic instability, which was predicted theoretically by Le Dizès (2008), is of much interest because it can be dominant depending on the parameter values. Its mechanism was identified successfully by the local stability analysis; namely, the resonance curve of the elliptic instability in the (β, θ_0) plane bends, eventually touching the line $\theta_0 = 0^\circ$, which happens for vortices with non-constant angular velocity (Hattori & Fukumoto 2003; Hattori & Hijiya 2010), so that it avoids the stabilizing effect of stratification. In this regard, the ring-type elliptic instability will also be observed for an isolated vortex in rotating stratified fluids under strain.

Some future works might be as follows. The effects of rotation and stratification on other flows possessing hyperbolic stagnation points, which include vortex pairs and wake vortices such as the von Kármán vortex street, are of interest. How each instability evolves in nonlinear regime is of great interest. Some of them can destroy vortices, while some can

promote merging of vortices or creation of strong vorticity (Hattori 2016, 2018), which will be studied by direct numerical simulation.

Funding. This work was supported by JSPS KAKENHI 17K05561. Numerical calculations were performed on AFI-NITY at the Institute of Fluid Science, Tohoku University.

Declaration of interests. The authors report no conflict of interest.

Author ORCIDs.
Yuji Hattori https://orcid.org/0000-0002-1601-6416.

References

Aravind, H.M., Dubos, T. & Mathur, M. 2022 Local stability analysis of homogeneous and stratified Kelvin–Helmholtz vortices. *J. Fluid Mech.* **943**, A18.

Arratia, C., Caulfield, C.P. & Chomaz, J.-M. 2013 Transient perturbation growth in time-dependent mixing layers. *J. Fluid Mech.* **717**, 90–133.

Aspden, J.M. & Vanneste, J. 2009 Elliptical instability of a rapidly rotating, strongly stratified fluid. *Phys. Fluids* **21**, 074104.

Bayly, B.J., Holm, D.D. & Lifschitz, A. 1996 Three-dimensional stability of elliptical vortex columns in external strain flows. *Phil. Trans. R. Soc. Lond.* A **354**, 895–926.

Billant, P. 2000 Zigzag instability of vortex pairs in stratified and rotating fluids. Part 1. General stability equations. *J. Fluid Mech.* **660**, 354–395.

Billant, P. & Chomaz, J.-M. 2000*a* Experimental evidence for a new instability of a vertical columnar vortex pair in a strongly stratified fluid. *J. Fluid Mech.* **418**, 167–188.

Billant, P. & Chomaz, J.-M. 2000*b* Theoretical analysis of the zigzag instability of a vertical columnar vortex pair in a strongly stratified fluid. *J. Fluid Mech.* **419**, 29–63.

Billant, P. & Chomaz, J.-M. 2000*c* Three-dimensional stability of a vertical columnar vortex pair in a stratified fluid. *J. Fluid Mech.* **419**, 65–91.

Billant, P., Deloncle, A., Chomaz, J.-M. & Otheguy, P. 2010 Zigzag instability of vortex pairs in stratified and rotating fluids. Part 2. Analytical and numerical analyses. *J. Fluid Mech.* **660**, 396–429.

Deloncle, A., Billant, P. & Chomaz, J.-M. 2008 Nonlinear evolution of the zigzag instability in stratified fluids: a shortcut on the route to dissipation. *J. Fluid Mech.* **599**, 229–239.

Donnadieu, C., Ortiz, S., Chomaz, J.-M. & Billant, P. 2009 Three-dimensional instabilities and transient growth of a counter-rotating vortex pair. *Phys. Fluids* **21**, 094102.

Edwards, W.S., Tuckerman, L.S., Friesner, R.A. & Sorensen, D.C. 1994 Krylov methods for the incompressible Navier–Stokes equations. *J. Comput. Phys.* **110**, 82–102.

Etling, D. 1989 On atmospheric vortex streets in the wake of large islands. *Meteorol. Atmos. Phys.* **41**, 157–164.

Friedlander, S. & Vishik, M.M. 1991 Instability criteria for the flow of an inviscid incompressible fluid. *Phys. Rev. Lett.* **66**, 2204–2206.

Gau, T. & Hattori, Y. 2014 Modal and non-modal stability of two-dimensional Taylor–Green vortices. *Fluid Dyn. Res.* **46**, 031410.

Godeferd, F.S., Cambon, C. & Leblanc, S. 2001 Zonal approach to centrifugal, elliptic and hyperbolic instabilities in Stuart vortices with external rotation. *J. Fluid Mech.* **449**, 1–37.

Guimbard, D., Le Dizès, S., Le Bars, M., Le Gal, P. & Leblanc, S. 2010 Elliptic instability of a stratified fluid in a rotating cylinder. *J. Fluid Mech.* **660**, 240–257.

Hattori, Y. 2016 Concentration of vorticity in a destabilized vortex due to selective decay. *J. Fluid Mech.* **797**, 630–643.

Hattori, Y. 2018 Concentration of vorticity due to selective decay in doubly periodic vortices and a vortex pair. *Fluid Dyn. Res.* **50**, 011405.

Hattori, Y. & Fukumoto, Y. 2003 Short-wavelength stability analysis of thin vortex rings. *Phys. Fluids* **15**, 3151–3163.

Hattori, Y. & Hijiya, K. 2010 Short-wavelength stability analysis of Hill's vortex with/without swirl. *Phys. Fluids* **20**, 074104.

Hattori, Y. & Hirota, M. 2023 Stability of two-dimensional Taylor–Green vortices in rotating stratified fluids. *J. Fluid Mech.* **967**, A32.

Hattori, Y., Suzuki, S., Hirota, M. & Khandelwal, M. 2021 Modal stability analysis of arrays of stably stratified vortices. *J. Fluid Mech.* **909**, A4.

JULIEN, S., ORTIZ, S. & CHOMAZ, J.-M. 2004 Secondary instability mechanisms in the wake of a flat plate. *Eur. J. Mech. (*B*/Fluids)* **23**, 157–165.

KLOOSTERZIEL, R.C. & VAN HEIJST, G.J.F. 1991 An experimental study of unstable barotropic vortices in a rotating fluid. *J. Fluid Mech.* **223**, 1–24.

LEBLANC, S. 1997 Stability of stagnation points in rotating flows. *Phys. Fluids* **9**, 3566–3569.

LEBLANC, S. 2000 Internal wave resonances in strain flows. *J. Fluid Mech.* **477**, 259–283.

LEBLANC, S. & CAMBON, C. 1998 Effects of the Coriolis force on the stability of Stuart vortices. *J. Fluid Mech.* **356**, 353–379.

LEBLANC, S. & GODEFERD, F.S. 1999 An illustration of the link between ribs and hyperbolic instability. *Phys. Fluids* **11**, 497–499.

LE DIZÈS, S. 2008 Inviscid waves on a Lamb–Oseen vortex in a rotating stratified fluid: consequences for the elliptic instability. *J. Fluid Mech.* **597**, 283–303.

LE DIZÈS, S. & BILLANT, P. 2009 Radiative instability in stratified vortices. *Phys. Fluids* **21**, 096602.

LEWEKE, T. & WILLIAMSON, C.H.K. 1998 Three-dimensional instabilities in wake transition. *Eur. J. Mech. (*B*/Fluids)* **17**, 571–586.

LIFSCHITZ, A. & HAMEIRI, E. 1991 Local stability conditions in fluid dynamics. *Phys. Fluids* A **3**, 2644–2651.

LIFSCHITZ, A. & HAMEIRI, E. 1993 Localized instabilities of vortex rings with swirl. *Commun. Pure Appl. Maths* **46**, 1379–1408.

MIYAZAKI, T. 1993 Elliptical instability in a stably stratified rotating fluid. *Phys. Fluids* A **5**, 2702–2709.

MIYAZAKI, T. & ADACHI, K. 1998 Short-wavelength instabilities of waves in rotating stratified fluids. *Phys. Fluids* **10**, 3168–3177.

MIYAZAKI, T. & FUKUMOTO, Y. 1992 Three-dimensional instability of strained vortices in a stably stratified flow. *Phys. Fluids* A **4**, 2515–2522.

OTHEGUY, P., BILLANT, P. & CHOMAZ, J.-M. 2006*a* Elliptic and zigzag instabilities on co-rotating vertical vortices in a stratified fluid. *J. Fluid Mech.* **553**, 253–272.

OTHEGUY, P., BILLANT, P. & CHOMAZ, J.-M. 2006*b* The effect of planetary rotation on the zigzag instability of co-rotating vortices in a stratified fluid. *J. Fluid Mech.* **553**, 273–281.

PARK, J. & BILLANT, P. 2013 Instabilities and waves on a columnar vortex in a strongly stratified and rotating fluid. *Phys. Fluids* **25**, 086601.

PEYRET, R. 2010 *Spectral Methods for Incompressible Viscous Flow*. Springer.

PIERREHUMBERT, R.T. & WIDNALL, S.E. 1982 The two- and three-dimensional instabilities of a spatially periodic shear layer. *J. Fluid Mech.* **114**, 59–82.

POTYLITSIN, P.G. & PELTIER, W.R. 1998 Stratification effects on the stability of columnar vortices on the f-plane. *J. Fluid Mech.* **355**, 45–79.

POTYLITSIN, P.G. & PELTIER, W.R. 1999 Three-dimensional destabilization of Stuart vortices: the influence of rotation and ellipticity. *J. Fluid Mech.* **387**, 205–226.

PRALITS, J.O., GIANNETTI, F. & BRANDT, L. 2013 Three-dimensional instability of the flow around a rotating circular cylinder. *J. Fluid Mech.* **730**, 5–18.

RAYLEIGH, LORD 1917 On the dynamics of revolving fluids. *Proc. R. Soc. Lond.* A **93**, 148–154.

SIPP, D. & JACQUIN, L. 1998 Elliptic instability in two-dimensional flattened Taylor–Green vortices. *Phys. Fluids* **10**, 839–849.

SIPP, D., LAUGA, E. & JACQUIN, L. 1999 Vortices in rotating systems: centrifugal, elliptic and hyperbolic type instabilities. *Phys. Fluids* **11**, 3716–3728.

STEGNER, A., PICHON, T. & BEUNIER, M. 2005 Elliptical-inertial instability of rotating Kármán vortex streets. *Phys. Fluids* **17**, 066602.

SUZUKI, S., HIROTA, M. & HATTORI, Y. 2018 Strato-hyperbolic instability: a new mechanism of instability in stably stratified vortices. *J. Fluid Mech.* **854**, 293–323.

THORPE, S.A. 2005 *The Turbulent Ocean*, chap. 13. Cambridge University Press.

WAITE, M.L. & SMOLARKIEWICZ, P.K. 2008 Instability and breakdown of a vertical vortex pair in a strongly stratified fluid. *J. Fluid Mech.* **606**, 239–273.

YIM, E. & BILLANT, P. 2016 Analogies and differences between the stability of an isolated pancake vortex and a columnar vortex in stratified fluid. *J. Fluid Mech.* **796**, 732–766.

YOUSSEF, A. & MARCUS, P.S. 2003 The dynamics of Jovian white ovals from formation to merger. *Icarus* **162**, 74–93.